SYNTHESIS AND INVESTIGATION OF FeNi AND FeCo BINARY NANOALLOY

RUBAYET TANVEER

(Student ID: 101440004)

A THESIS SUBMITTED

FOR THE DEGREE OF MASTER OF

PHILOSOPHY IN PHYSICS

DEPARTMENT OF SCENCE AND HUMANITIES

MILITARY INSTITUTE OF SCIENCE AND

TECHNOLOGY

2019

DECLARATION

"I hereby declare that this thesis is my original work and it has been written by me in its entirety. I have duly acknowledged all the sources of information which have been used in the thesis. This thesis has also not been submitted for any degree in any university previously."

_____

Rubayet Tanveer

Student ID: 101440004

April 2019

ACKNOWLEDGEMENTS

At first, I fervently express all of my admiration and devotion to the almighty ALLAH, the most beneficial who has enabled me to perform this research work and to submit this thesis.

With much pleasure, I respectfully express my earnest gratitude to my honorable teacher and supervisor Major Brajalal Sinha, PhD, Department of Science and Humanities, Military Institute of Science and Technology (MIST) for his scholastic guidance, instructions, valuable advice, suggestions, relentless patience and continuous encouragement throughout my voyage of research.

I express my profound gratitude to my honorable co-supervisor Professor Dr. Mohammed Abdul Basith, Department of Physics, Bangladesh University of Engineering and Technology (BUET), for his constant direction, constructive criticism and inspiration in pursuing the whole investigation of the present research. Words are always insufficient to express his working capacities and unending enthusiasm for scientific rigorousness for innovative investigations. This always becomes everlasting source of inspiration for his students.

I would also like to express my humblest thanks to Dr. Sri Ramulu Torati, Research Professor, Department of Emerging Materials Science, DGIST, South Korea for providing me with experimental facilities to carry out XRD, FESEM, EDS and VSM measurements of my samples during this research.

Next, I offer my gratefulness to Captain M Ziaul Ahsan (retired), BN, Ex-Head, Department of Science and Humanities and Wing Commander Md Nurul Huda, Head, Department of Science and Humanities, MIST for their kind permission to perform this work. I thank my respected teacher

Major Md. Mahabubar Rahman Shah, PhD for his constant help throughout the completion of the degree. I am also grateful to MIST authority for providing the financial grant for this research.

I am also grateful to Mr. Galib Hashmi who is a PhD student in Department of EEE at University of Dhaka and also my undergrad project supervisor for his guidance, inspiration and encouragement. I wish to give special thanks to Arif Khan and Lieutenant Sonjibone Sudha, (ND), BN my fellow M.Phil. Researchers for their constant support. I also thank all the staffs of Physics lab for their constant help while conducting my experimental works.

I am earnestly thankful to The World Academy of Sciences, Italy for supporting our work with Grant 14-024 RG/PHY/AS_I-UNESCO FR: 324028590.

Finally, I would mention a very special gratefulness for the moral support and sustaining inspiration provided by my family members.

(Rubayet Tanveer)

Author

CONTENTS

Acknowledgements IV

Index VI

List of Figures X

List of Tables XIII

Abstract XIV

CHAPTER 1

GENERAL INTRODUCTION

1.1 Introduction 01

1.2 Objectives of this Research 04

1.3 Outline of the Thesis 04

References 06

CHAPETER 2

LITERATURE REVIEW

2.1 Introduction 09

2.2 Magnetism 09

2.2.1 Diamagnetism 10

2.2.2 Paramagnetism 11

2.2.3 Ferromagnetism 12

2.2.3.1 Spontaneous Magnetization 14

2.2.3.2 Curie Temperature 15
2.2.3.3 Hysteresis 15
2.2.4 Ferrimagnetism 16
2.2.5 Antiferromagnetism 17
2.3 Nanomagnetism 18
2.3.1 Superparamagnetism 20
2.4 Synthesis of Magnetic Nanostructures 21
2.4.1 Chemical Synthesis 21
2.4.1.1 Thermal Decomposition 22
2.4.1.2 Hydrothermal Synthesis 23
2.4.1.3 Sol-gel Synthesis 23
2.4.2 Solid State Synthesis 24
2.4.2.1 Ball Milling 25
2.4.2.2 Sonofragmentation 25
References 26

CHAPTER 3

SAMPLE PREPARATION

3.1 Introduction 31
3.2 Materials and method 31
3.2.1 Ultrasonication Technique 32
3.2.2 Sonication Effects on Particle Disruption and Aggregation 36
References 38

CHAPTER 4

EXPERIMENTAL TECHNIQUES

4.1	Introduction	39
4.2	X-ray Diffraction	39
	4.2.1 Crystallite Size Measurement	41
4.3	Surface Morphology and Microstructure	44
	4.3.1 Scanning Electron Microscope (SEM)	44
	4.3.2 Scanning Process and Image Formation	47
4.4	Energy Dispersive Analysis by X-rays	48
4.5	Magnetization Measurement	49
	References	51

CHAPTER 5

RESULTS AND DISCUSSION

5.1	Crystallography Study	52
	5.1.1 X-ray diffraction Analysis of Fe_xNi_{100-x}	52
	5.1.2 X-ray diffraction Analysis of Fe_xCo_{100-x}	53
5.2	Microstructure Analysis	55
	5.2.1 FE-SEM Analysis of Fe_xNi_{100-x}	55
	5.2.2 FE-SEM Analysis of Fe_xCo_{100-x}	56
5.3	Elemental Analysis	57
	5.3.1 EDS Analysis of Fe_xNi_{100-x}	57
	5.3.2 EDS Analysis of Fe_xCo_{100-x}	58
5.4	Magnetic Properties	59

	5.4.1 VSM Analysis of Fe_xNi_{100-x}	59
	5.4.2 VSM Analysis of Fe_xCo_{100-x}	62
5.5	Additional Work	65
	5.5.1 X-ray diffraction Analysis of $Fe_{20}Ni_{80-x}Co_x$	65
	5.5.2 FE-SEM Analysis of $Fe_{20}Ni_{80-x}Co_x$	67
	5.5.3 EDS Analysis of $Fe_{20}Ni_{80-x}Co_x$	68
	5.5.4 VSM Analysis of $Fe_{20}Ni_{80-x}Co_x$	69
	References	73

CHAPTER 6

CONCLUSION

6.1	Overview	76
6.2	Limitations	77
6.3	Future Work	77

List of Figures

Figure 2.1	Diamagnetism explained with M-H curve, Susceptibility (left) and domain alignment (right).	10
Figure 2.2	Paramagnetism explained with M-H curve, Susceptibility (left) and domain alignment (right).	11
Figure 2.3	Domain alignment in ferromagnetism.	13
Figure 2.4	Spontaneous magnetization: (a) organization of magnetic domains for ferromagnetic materials and (b) arrangement of Weiss domains as a function of applied magnetic field (H) with different intensities.	13
Figure 2.5	Figure 2.5: Hysteresis Loop.	16
Figure 2.6	Domain alignment in ferromagnetic materials.	17
Figure 2.7	Domain alignment (left) and susceptibility as function of temperature (right) of antiferromagnetism.	18
Figure 2.8	Figure 2.8: Size dependent coercivity of magnets.	19
Figure 2.9	Schematic behavior of (a) Diamagnetic, (b) Paramagnetic, (c) Ferromagnetic, (d) Superparamagnetic materials in an external magnetic field.	20
Figure 2.10	LaMer and Dinegar model.	22
Figure 2.11	General steps of hydrothermal synthesis.	23
Figure 2.12	The reaction pathway for the production of nanostructures in the Sol–gel method.	24
Figure 2.13	Schematic motion of the ball milling powder mixture.	25
Figure 3.1	Sample preparation method.	32
Figure 3.2	Schematic illustration of ultrasonic wave-induced cavitation and agglomerate fracture.	33

Figure 3.3	Schematic illustration of direct (left) and indirect (middle and right) sonication con- gurations as described in the text.	34
Figure 3.4	Schematic depiction of particle structures referred to in the text, and illustration of the typical effects of sonication on particle size as a function of delivered sonication energy.	37
Figure 4.1	Bragg's law of X-ray diffraction.	40
Figure 4.2	Effect of fine particle size on diffraction curves (Schematic): (a) small particle size and (b) large particle size.	42
Figure 4.3	Schematic diagram of SEM setup.	45
Figure 4.4	Scanning Electron Microscopy. (SEM).	46
Figure 4.5	Schematic representation of EDS Instrument.	48
Figure 4.6	Block diagram of VSM.	49
Figure 4.7	Vibrating Sample Magnetometer (VSM)	50
Figure 5.1	XRD pattern (from bottom to up) of $Fe_{20}Ni_{80}$, $Fe_{60}Ni_{40}$ and $Fe_{80}Ni_{20}$ binary nanoalloy.	53
Figure 5.2	XRD pattern (from bottom to up) of $Fe_{20}Co_{80}$, $Fe_{60}Co_{40}$ and $Fe_{80}Co_{20}$ binary nanoalloy.	54
Figure 5.3.	FE-SEM images of (a) $Fe_{20}Ni_{80}$, (b) $Fe_{40}Ni_{60}$, (c) $Fe_{80}Ni_{20,}$ (d) particle size distribution.	55
Figure 5.4	FE-SEM images of (a) $Fe_{20}Co_{80}$, (b) $Fe_{40}Co_{60}$, (c) $Fe_{80}Co_{20}$ and (d) particle size distribution.	56
Figure 5.5	EDS spectra for $Ni_{80}Fe_{20}$.	57
Figure 5.6	EDS spectra for $Fe_{80}Co_{20}$.	58

Figure 5.7	EDS mapping analysis of $Fe_{80}Co_{20}$; (a) SEM image of $Fe_{80}Co_{20}$ nanoalloy to be analyzed for mapping (b) map of Fe concentration (c) map of Co concentration (d) EDS mapping image of $Fe_{80}Co_{20}$ nanoalloy.	59
Figure 5.8	Magnetization versus magnetic field curves of $Ni_{1-x}Fe_x$ nanoalloy.	60
Figure 5.9	Variation of saturation magnetization and coercivity with Fe in $Ni_{1-x}Fe_x$ nanoalloy.	61
Figure 5.10	Magnetization versus magnetic field curves of Fe_xCo_{1-x} nanoalloy.	63
Figure 5.11	Variation of saturation magnetization and coercivity with Fe in FexCo1-x nanoalloy.	63
Figure 5.12	XRD pattern of $Fe_{20}Ni_{80-x}Co_x$ ternary nanoalloy.	66
Figure 5.13	FE-SEM images of $Fe_{20}Ni_{80-x}Co_x$, (a) x=20, (b) x=40, (c) x=60, (d) Particle size distribution in Figure (a).	67
Figure 5.14	EDS spectra for $Fe_{20}Co_{20}Ni_{60.}$	68
Figure 5.15	The EDS map of the $Fe_{20}Co_{20}Ni_{60}$ particles.	69
Figure 5.16	Magnetization versus magnetic field curves of $Fe_{20}Ni_{80-x}Co_x$ (x = 20, 40 and 60) nanoalloy.	70

List of Tables

Table 1.1	Drawbacks of various nanoparticle synthesis techniques.	3
Table 2.1	Paramagnetic and ferromagnetic susceptibility.	14
Table 5.1	Comparative study of reported magnetic properties of Ni-Fe nanoalloys prepared by using different synthesis methods.	62
Table 5.2	Different parameters of magnetic properties for Fe_xCo_{1-x} nanoalloy.	64
Table 5.3	Comparative study of reported magnetic properties of Fe-Co nanoalloys at room temperature prepared by using different synthesis methods.	64
Table 5.4	Composition, FWHM, crystallite size and lattice constant of $Fe_{20}Ni_{80-x}Co_x$, x = 20, 40 and 60.	66
Table 5.5	Composition, coercivity, saturation magnetization and reduced remanence of $Fe_{20}Ni_{80-x}Co_x$, x = 20, 40 and 60.	71
Table 5.6	Comparative study of reported magnetic properties of Fe-Ni-Co nanoalloys prepared via different synthesis methods.	72

ABSTRACT

Fe_xNi_{100-x} and Fe_xCo_{100-x} (x = 20, 40 and 80) alloy nanoparticles (NPs) were synthesized by sonofragmentation process, a facile one-step technique to produce NPs directly from bulk powders. The structural properties were studied by using X-ray Diffraction (XRD). The XRD shows the crystalline structure of the alloy samples and the size of the crystallites were calculated 35 nm and 19.3 nm for Fe-Ni and Fe-Co respectively with significant amount of phase purity. The compositions of Ni, Fe and Co in the alloy are confirmed from energy dispersive spectroscopy (EDS). It also reveals that there is no unwanted element in the alloys. Scanning electron microscopy (SEM) reveals the aggregation or cluster of spherical NPs with wide size distribution from 20 to 50 nm for all compositions of nanoalloys. The vibrating sample magnetometer (VSM) illustrates the superparamagnetic behavior of the alloys. The saturation magnetization (M_s) is found to be 57, 66 and 105 emu/g for $Fe_{20}Ni_{80}$, $Fe_{40}Ni_{60}$ and $Fe_{80}Ni_{20}$ NPs alloys respectively. The values of M_s were found to be 107, 131, and 153 emu/g for $Fe_{20}Co_{80}$, $Fe_{40}Co_{60}$ and $Fe_{80}Co_{20}$ NPs alloys respectively. However, the coercivity (H_c) is observed 73, 64 and 57 Oe for $Fe_{20}Ni_{80}$, $Fe_{40}Ni_{60}$ and $Fe_{80}Ni_{20}$ respectively. The value of H_c is also observed 128, 113 and 72 Oe for $Fe_{20}Co_{80}$, $Fe_{40}Co_{60}$ and $Fe_{80}Co_{20}$ respectively. It can be noticed that with increasing Fe content magnetization increases whereas corercivity decreases. The increasing magnetization may be ascribed to the incorporation of higher magnetic moments into the compositions. Such compositional dependent nature shows an important approach to attain tunable magnetic properties of Fe-Ni and Fe-Co NPs for their many practical applications. Moreover, the synthesized high magnetization Fe-Ni and Fe-Co nanoalloy can be used for

various potential applications, and also this simple and environment friendly technique can be extended to synthesize other nanostructures.

CHAPTER 1

GENERAL INTRODUCTION

1.1 Introduction

Magnetic nanoparticles (NPs) are a topic of increasing research interest due to their versatile applications in magnetic recording devices, drug delivery, magnetic separation, MRI contrast enhancement, magnetic fluids, hyperthermia, magnetic sensors, catalysis, microwave absorbers, inductor cores [1-7]. Monodisperse magnetic nanoparticles are of potential elements for using in ultrahigh magnetic recording while superparamagnetic nanoparticles are mostly deployed in biomedical applications such as MRI contrast enhancement and cancer hyperthermia treatment [8]. To enhance the efficiency of such applications, magnetic properties of the nanoparticles have been tuned by various strategies including changing the composition of various elements or doping by other magnetic or non-magnetic elements [8-9].

The development of bimetallic NPs (alloy) based on Fe, Co, and Ni has received much recent attention because of their novel catalytic, magnetic, and optical properties, which could be considerably different from those of their constituent single metallic materials [3, 6]. Among various ferromagnetic nanoparticles, iron-based nanocrystalline alloys have shown significant potential in diversified applications such as electric or magnetic measurements, information storage, and magnetic refrigeration because of their high magnetization and low coercivity [10]. Addition of Ni and Co may further improve the high-temperature magnetic properties of these Fe-based amorphous alloys [11]. Especially, Fe-Co alloy has attracted significant research interest due to their unique magnetic properties such as high saturation magnetization, high Curie

temperature and large permeability and low hysteresis loss [1, 4-5]. For the application of the miniaturized high density recording device, higher saturation magnetization and appropriate coercive force are required to easily flip the direction of magnetization in the miniaturized high density recording device [12]. Cobalt in iron has been shown to have a unique effect in simultaneous increasing of the saturation magnetization and Curie temperature [13]. Moreover, inclusion of Ni to Fe–Co alloys increases permeability and electrical resistivity properties which have great importance for write head core materials [13]. This Fe-Ni-Co ternary alloy is recognized as magnetically soft and prospective magnetic material with excellent thermal stability [14-15]. Also Fe-Ni-Co alloy has magnetostrictive properties so it can be used for making the magneto-resistance element such as a magneto-resistance sensor, a magneto-resistance head, etc. [16]. Therefore, alloys containing transition elements like Fe, Ni, and Co should get significant attention and their microstructure must be studied meticulously because of their fascinating magnetic properties and potential applicability [11, 17].

Recently, various attempts to synthesize magnetic NPs have been reported including ball milling, chemical reduction, hydrothermal, thermal decomposition, microemulsion, solution phase reduction, wet chemistry and chemical vapor deposition. Although, all of the above reported methods in some way significantly participate to synthesize magnetic NPs with different shapes and size with controlled composition, however, the usage of toxic chemicals and complex synthesis process limits their use in practical applications. In addition, the involvement of high cost and time consuming steps (see Table 1.1) also remain as a challenge for synthesis of ferromangnetic NPs. Thus, there is a need for the development of facile synthesis approach for magnetic NPs with environment friendly and cost-effective. On the other hand, recently the

sonofragmentation method, which is a one-step, facile, low cost and environment friendly technique, has been used for the preparation of NPs directly from bulk materials [1].

Table 1.1: Drawbacks of various nanoparticle synthesis techniques.

Different Synthesis Techniques	Drawbacks
Ball Milling	▪ Contamination from milling tools and ambient gases [18]. ▪ Long Processing time, agglomeration, and increased crystal defect density and surface roughness of synthesized nanoparticles [18,19].
Chemical Vapor Deposition (CVD)	▪ High temperature, high Vacuum, high cost [20]. ▪ Relatively complicated experiments [20].
Wet Chemical (Sol-gel, Hydrothermal etc.)	▪ Use of various toxic precursors [21]. ▪ Complex solution process [21]. ▪ Time control [20].

Hence, magnetic nanoalloys can be synthesized by using facile sonofragmentation approach with inexpensive way. In this thesis, we report a simple cost-effective and ecofriendly sonofragmentation technique to synthesize bimetallic Fe_xNi_{100-x} and Fe_xCo_{100-x} (x = 20, 40 and 80) nanoalloy particles with controlled saturation magnetization and coercivity by changing the precursor materials. By increasing the Fe content in the vicinity of both Fe-Ni and Fe-Co nanoalloy, the values of saturation magnetization (Ms) are found to be increasing whereas coercivity decreasing. Various characterization techniques are used for the analysis of the synthesized nanoalloy. The morphological and crystalline structures were observed by field emission scanning electron microscopy (FE-SEM) and X-ray diffraction (XRD) pattern, respectively. The elemental composition was analyzed by energy-dispersive spectroscopy (EDS)

coupled with FE-SEM. The magnetic properties of the synthesized samples at room temperature were investigated using a vibrating sample magnetometer (VSM) respectively.

1.2 Objectives of this Research

The main Objectives of this research are as follows:

(a) Preparation of compositions of Fe_xNi_{100-x} and Fe_xCo_{100-x} (x = 20, 40 and 80) compositions of bulk polycrystalline powders by using manual grinding.

(b) Production of nanoparticles from those bulk powder materials using sonofragmentation technique.

(c) Analysis of the crystal structure of the sonicated nanoparticles using X-ray diffraction (XRD) techniques.

(d) Investigation of the surface morphology of the as prepared sample using Field Emission Scanning Electron Microscopy (FESEM).

(e) To confirm the elemental analysis and study the percentages of impurities using Energy Dispersive Spectroscopy (EDS).

(f) Measurements of the magnetic properties such as saturation magnetization (M_s), and coercivity (H_c) of Fe_xNi_{100-x}, Fe_xCo_{100-x} (x = 20, 40 and 80) and nanoparticles from hysteresis loops by using Vibrating Sample Magnetometer (VSM).

1.3 Outline of the Thesis

The thesis is organized as follows:

- **Chapter 1** of this thesis deals with the background of the research, importance of Magnetic materials, importance of the sonofragmentation synthesis method, significance and objectives of the present work.

- **Chapter 2** gives a brief overview of the theoretical background.
- **Chapter 3** provides the details of the sample preparation.
- **Chapter 4** provides the description of different measurement techniques that have been used in this research work.
- **Chapter 5** is dedicated to the results of various investigations of the study and explanation of results in the light of existing theories.
- The conclusions drawn from the overall experimental results and discussions are presented in **Chapter 6.**

References

[1] Sinha B., Tanveer R., Torati S. R., Ahsan M. Z., Shah M. R., Basith M. A., Simple sonofragmentation approach for synthesis of Ni-Fe nanoalloy with tunable magnetization, *IEEE Magnetics Letters*, vol. 8 (2017), 4108404.

[2] Schooneveld M. M. V., Campos-Cuerva C., Pet J., Meeldijk J. D., Rijssel, Meijerink J. V., Erne A, B. H., Groot F. M. F. D, Composition tunable cobalt-nickel and cobalt-iron alloy nanoparticles below 10 nm synthesized using acetonated cobalt carbonyl, *J. Nanoparticle Res.*, vol. 14 (2012), 991.

[3] Moghimi N.,Bazargan S.,Pradhan D.,Leung K. T., Phase-induced shape evolution of FeNi nanoalloys and their air stability by in-situ surface passivation, *J. Phys. Chem. C*, vol. 117 (2013), 4852–4858.

[4] Shokuhfar A., Afghahi S. S. S., Size controlled synthesis of FeCo nanoparticles and study of the particle size and distribution effects on magnetic properties, *Adv. Mater. Sci. Eng*. (2014), 295390.

[5] Kandapallil B., Colborn R. E., Bonitatibus P. J., Johnson F., Synthesis of high magnetization Fe and FeCo nanoparticles by high temperature chemical reduction, *J. Magn. Magn. Mater*., vol. 378 (2015), 535–538.

[6] Sharma H., Jain S., Raj P. M., Murali K. P., Tummala R., Magnetic and dielectric property studies in Fe- and Ni-Fe based polymer nanocomposites, *J. Electron. Mater*., vol. 44 (2015), 3819–3826.

[7] Ishizaki T., Yatsugi K.,Akedo K., Effect of particle size on the magnetic properties of Ni nanoparticles synthesized with trioctylphosphine as the capping agent, *Nanomaterials*, vol. 6 (2016), 172.

[8] Chokprasombat K., Pinitsoontorn S., Maensiri S., Effects of Ni content on nanocrystalline Fe-Ni-Coternary alloys synthesized by a chemical reduction method, *J. of Magn. Magn. Mater*., vol. 405 (2016) 174–180.

[9] Kolhatkar A. G., Jamison A. C., Litvinov D., Willson R. C., Lee T. R., Tuning the magnetic properties of nanoparticles, *Int. J. Mol. Sci.* 14 (2013), 15977-16009.

[10] Shokrollahi H., The magnetic and structural properties of most important alloys of iron produced by mechanical alloying. *Mater. Des*. 30 (2009), 3374–3387.

[11] Prasad N. K., Kumar V., Structure–magnetic properties correlation in mechanically alloyed nanocrystalline Fe–Co–Ni–$(Mg–Si)_x$ alloy powders, *J. Mater. Sci.: Mater Electron* (2016), DOI 10.1007/s10854-016-5090-4.

[12] Park J. H., Kweon S. C., Kim S. W., Structural and magnetic properties of electrospun Fe-Ni-Co magnetic nanofibers with nanogranular phases, *J. Nanopart. Res*., 14 (2012), 729.

[13] Baghbaderani H. A., Sharafi S., Chermahini M. D., Investigation of nanostructure formation mechanism and magnetic properties in $Fe_{45}Co_{45}Ni_{10}$ system synthesized by mechanical alloying, *Powder Technology*, 230 (2012) 241–246.

[14] Sharma G., Grimes C. A., Synthesis, characterization, and magnetic properties of FeCoNi ternary alloy nanowire arrays, *J. Mater. Res*., vol. 19 (2004), 3695.

[15] Budi S., Hafizah M. E., Manaf A., Synthesis of FeCoNi nanoparticles by galvanostatic technique, *AIP Conf. Proc.*, 1746 (2016), 020012.

[16] Pikula T., Oleszak D., Pekata M., Jartych E., Structure and some magnetic properties of mechanically synthesized and thermally treated Co–Fe–Ni alloys, *J. Magn. Magn. Mater*. 320 (2008) 413–420.

[17] Bahgat M., Paek M. K., Pak J. J., Comparative synthesize of nanocrystalline Fe–Ni and Fe–Ni–Co alloys during hydrogen reduction of $Ni_xCo_{1-x}Fe_2O_4$, *J. Alloys Compd*., 466 (2008), 59–66.

[18] Cao W., Synthesis of nanomaterials by high energy ball Milling, *Skyspring Nanomaterials, Inc.,* www.understandingnano.com/nanomaterial-synthesis-ball-milling.html.

[19] Basith M. A, Islam M. A., Bashir Ahmmad, Sarowar Hossain M. D., Mølhave K., Preparation of high crystalline nanoparticles of rare-earth based complex pervoskites and comparison of their structural and magnetic properties with bulk counterparts, *Materials Research Express*, 4 (2017), Number 7.

[20] Chaoliang T., Zhang H., Wet-chemical synthesis and applications of non-layer structured two-dimensional nanomaterials, *Nature Communications*, 6 (2015), Article number 7873.

[21] Basith M. A., Ngo D. T., Quader A., Rahman M. A., Sinha B. L., Ahmmad B., Simple top-down preparation of magnetic $Bi_{0.9}Gd_{0.1}Fe_{1-x}Ti_xO_3$ nanoparticles by ultrasonication of multiferroic bulk material, Nanoscale 6 (2014), 23, 14336-14342.

CHAPETER 2

LITERATURE REVIEW

2.1 Introduction

The history of magnetism is coeval with the history of science. The magnet's ability to attract ferrous objects by remote control, acting at a distance, has captivated countless curious spirits over two millennia [1]. Also what deviations occurs to these properties when the magnet is nanostructured or how the nanostructured magnets are synthesized. These fundamental issues are the subject of this chapter.

2.2 Magnetism

The origin of magnetism lies in the orbital and spin motions of electrons and how the electrons interact with one another. The best way to introduce the different types of magnetism is to describe how materials respond to magnetic fields. This may be surprising to some, but all matter is magnetic. It's just that some materials are much more magnetic than others. The main distinction is that in some materials there is no collective interaction of atomic magnetic moments, whereas in other materials there is a very strong interaction between atomic moments. The magnetic behavior of materials can be classified into the following five major groups:

- Diamagnetism
- Paramagnetism
- Ferromagnetism
- Ferrimagnetism
- Antiferromagnetism

Materials in the first two groups are those that exhibit no collective magnetic interactions and are not magnetically ordered. Materials in the last three groups exhibit long-range magnetic order below a certain critical temperature. Ferromagnetic and ferrimagnetic materials are usually what we consider as being magnetic (i.e., behaving like iron). The remaining three are so weakly magnetic that they are usually thought of as "nonmagnetic".

2.2.1 Diamagnetism

Diamagnetism is a fundamental property of all matter, although it is usually very weak. It is due to the non-cooperative behavior of orbiting electrons when exposed to an applied magnetic field. Diamagnetic substances are composed of atoms which have no net magnetic moments (i.e., all the orbital shells are filled and there are no unpaired electrons).

However, when exposed to a field (H), a negative magnetization (M) is produced and thus the susceptibility (χ) is negative. If we plot M vs. H, we see:

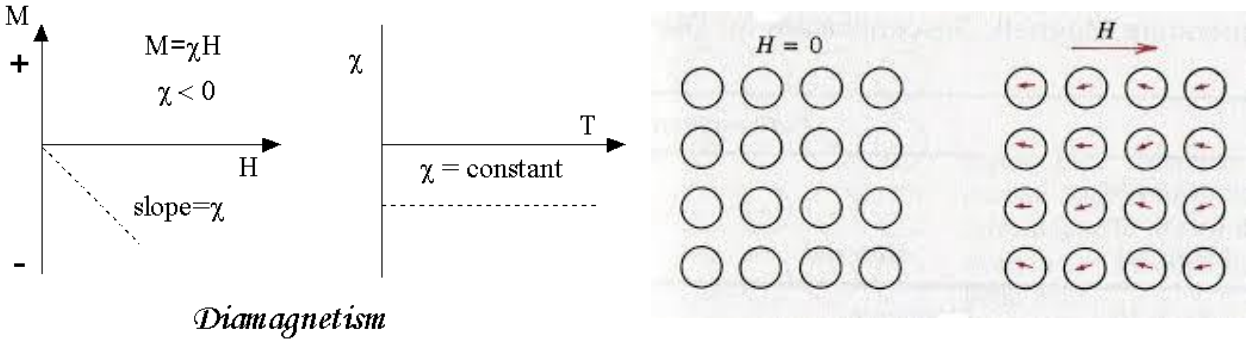

Figure 2.1: Diamagnetism explained with M-H curve, Susceptibility (left) and domain alignment (right).

To be noticed from Figure 2.1 that when the field is zero the magnetization is zero. The other characteristic behavior of diamagnetic materials is that the susceptibility (χ) is temperature (T) independent. Some well-known diamagnetic substances, include:

- Quartz (SiO_2)
- Calcite ($CaCO_3$)
- Water

2.2.2 Paramagnetism

This class of materials, some of the atoms or ions in the material has a net magnetic moment due to unpaired electrons in partially filled orbitals. One of the most important atoms with unpaired electrons is iron. However, the individual magnetic moments do not interact magnetically, and like diamagnetism, the magnetization is zero when the field is removed. In the presence of a field, there is now a partial alignment of the atomic magnetic moments in the direction of the field, resulting in a net positive magnetization and positive susceptibility (Figure 2.2).

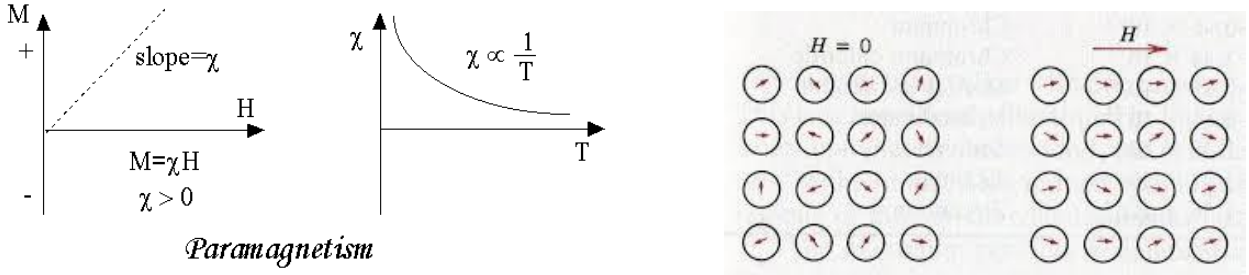

Figure 2.2: Paramagnetism explained with M-H curve, Susceptibility (left) and domain alignment (right).

In addition, the efficiency of the field in aligning the moments is opposed by the randomizing effects of temperature. This results in a temperature dependent susceptibility, known as the Curie Law.

At normal temperatures and in moderate fields, the paramagnetic susceptibility is small (but larger than the diamagnetic contribution). Unless the temperature is very low (<<100 K) or the field is very high paramagnetic susceptibility is independent of the applied field. Under these conditions, paramagnetic susceptibility is proportional to the total iron content. Many iron bearing minerals are paramagnetic at room temperature. Some examples, include:

- Montmorillonite (clay)
- Nontronite (Fe-rich clay)
- Biotite (silicate)
- Siderite (carbonate)
- Pyrite (sulfide)

The paramagnetism of the matrix minerals in natural samples can be significant if the concentration of magnetite is very small. In this case, a paramagnetic correction may be needed.

2.2.3 Ferromagnetism

Unlike paramagnetic materials, the atomic moments in these materials exhibit very strong interactions. These interactions are produced by electronic exchange forces and result in a parallel or anti-parallel alignment of atomic moments. Exchange forces are very large, equivalent to a field on the order of 1000 Tesla, or approximately a 100 million times the strength of the earth's field. The exchange force is a quantum mechanical phenomenon due to the relative orientation of the

spins of two electrons. Ferromagnetic materials exhibit parallel alignment of moments resulting in large net magnetization even in the absence of a magnetic field (Figure 2.3).

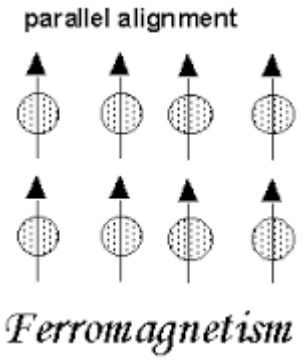

Figure 2.3: Domain alignment in ferromagnetism.

The elements Fe, Ni, and Co and many of their alloys are typical ferromagnetic materials. Two distinct characteristics of ferromagnetic materials are their

- Spontaneous magnetization.
- Magnetic ordering temperature.

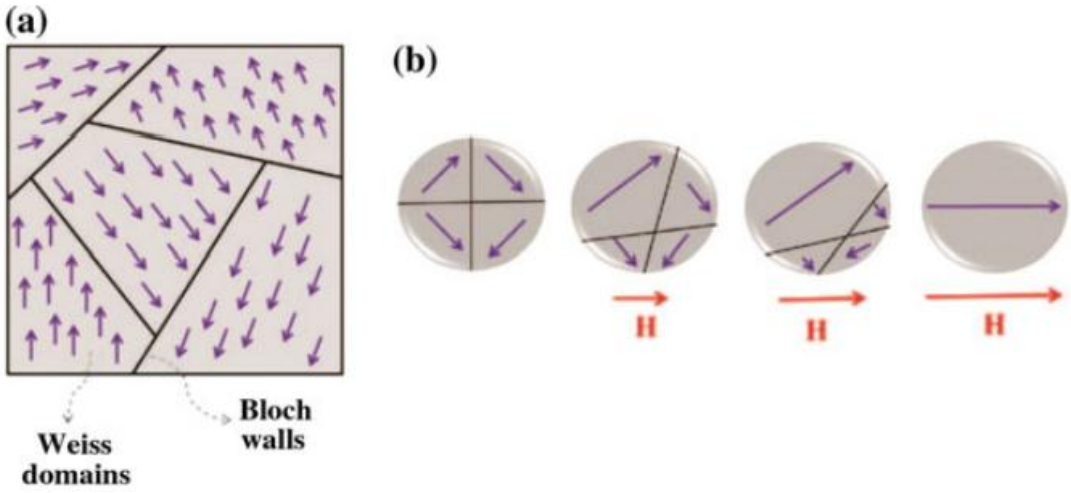

Figure 2.4: Spontaneous magnetization: **(a)** organization of magnetic domains for ferromagnetic materials and **(b)** arrangement of Weiss domains as a function of applied magnetic field (H) with different intensities.

2.2.3.1 Spontaneous Magnetization

The spontaneous magnetization (see Figure 2.4) is the net magnetization that exists inside a uniformly magnetized microscopic volume in the absence of a field. The magnitude of this magnetization, at 0 K, is dependent on the spin magnetic moments of electrons. A related term is the saturation magnetization which we can measure in the laboratory. The saturation magnetization is the maximum induced magnetic moment that can be obtained in a magnetic field (H_{sat}); beyond this field no further increase in magnetization occurs.

The difference between spontaneous magnetization and the saturation magnetization has to do with magnetic domains (more about domains later). Saturation magnetization is an intrinsic property, independent of particle size but dependent on temperature. There is a big difference between paramagnetic and ferromagnetic susceptibility. As compared to paramagnetic materials, the magnetization in ferromagnetic materials is saturated in moderate magnetic fields and at high (room-temperature) temperatures:

Table 2.1: Paramagnetic and ferromagnetic susceptibility.

	H_{sat} Oerested (Oe)	T range (K)	χ 10-6 cm3/g
Paramagnets	>100000	<<100	>1
Ferromagnets	~10000	~300	1-100000

2.2.3.2 Curie Temperature

Even though electronic exchange forces in ferromagnets are very large, thermal energy eventually overcomes the exchange and produces a randomizing effect. This occurs at a particular temperature called the Curie temperature (T_c). Below the Curie temperature, the ferromagnet is ordered and above it, disordered. The saturation magnetization goes to zero at the Curie temperature. The Curie temperature is also an intrinsic property and is a diagnostic parameter that can be used for mineral identification. However, it is not foolproof because different magnetic minerals, in principle, can have the same Curie temperature.

2.2.3.3 Hysteresis

In addition to the Curie temperature and saturation magnetization (M_s), ferromagnets can retain a memory of an applied field once it is removed. This behavior is called hysteresis and a plot of the variation of magnetization (M) with magnetic field (H) is called a hysteresis loop.

Another hysteresis property is the coercivity of remanence (H_r). This is the reverse field which, when applied and then removed, reduces the saturation remanence to zero. It is always larger than the coercive field (H_c). The initial susceptibility (χ_0) is the magnetization observed in low fields, on the order of the earth's field (0.5-1.0 Oe). The various hysteresis parameters are not solely intrinsic properties but are dependent on grain size, domain state, stresses, and temperature. Because hysteresis parameters are dependent on grain size, they are useful for magnetic grain sizing of natural samples.

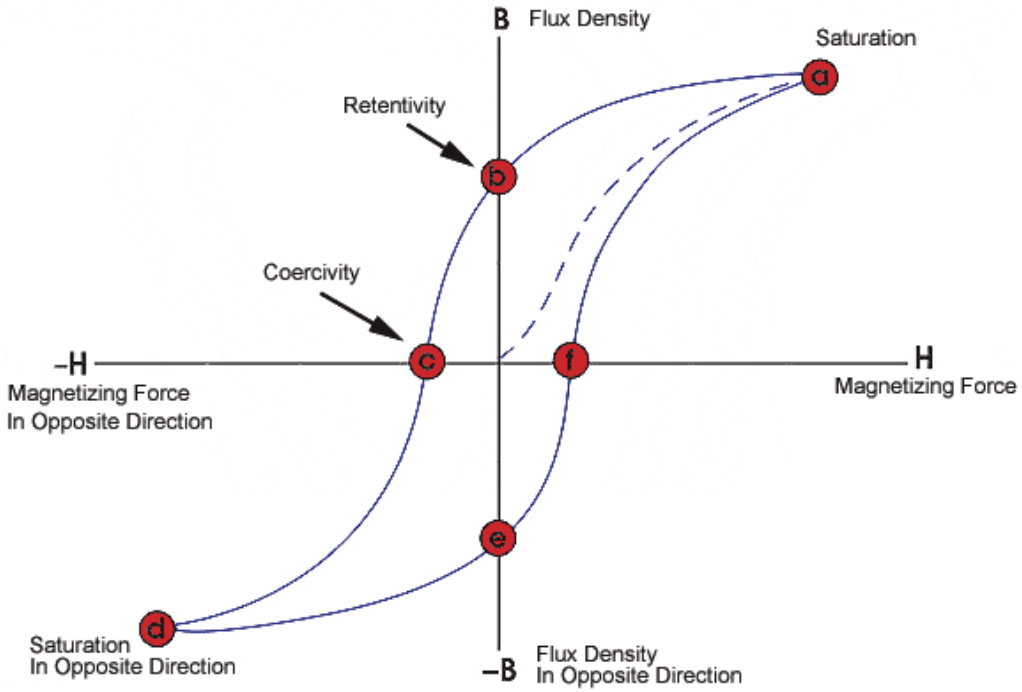

Figure 2.5: Hysteresis Loop.

2.2.4 Ferrimagnetism

In ionic compounds, such as oxides, more complex forms of magnetic ordering can occur as a result of the crystal structure. One type of magnetic ordering is call ferrimagnetism. A simple representation of the magnetic spins in a ferrimagnetic oxide is shown in Figure 2.6.

The magnetic structure is composed of two magnetic sublattices separated by oxygens. The exchange interactions are mediated by the oxygen anions. When this happens, the interactions are called indirect or superexchange interactions. The strongest superexchange interactions result in an antiparallel alignment of spins between the sublattices.

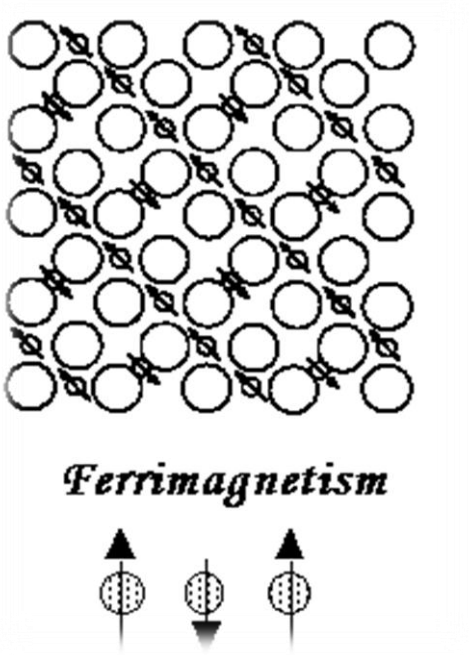

Figure 2.6: Domain alignment in ferromagnetic materials.

In ferrimagnets, the magnetic moments of the sublattices are not equal and result in a net magnetic moment. Ferrimagnetism is therefore similar to ferromagnetism. It exhibits all the hallmarks of ferromagnetic behavior- spontaneous magnetization, Curie temperatures, hysteresis, and remanence. However, ferro- and ferrimagnets have very different magnetic ordering.

Magnetite is a well-known ferrimagnetic material. Indeed, magnetite was considered a ferromagnet until Néel in the 1940's, provided the theoretical framework for understanding ferrimagnetism.

2.2.5 Antiferromagnetism

If the sublattice moments are exactly equal but opposite, the net moment is zero. This type of magnetic ordering is called antiferromagnetism.

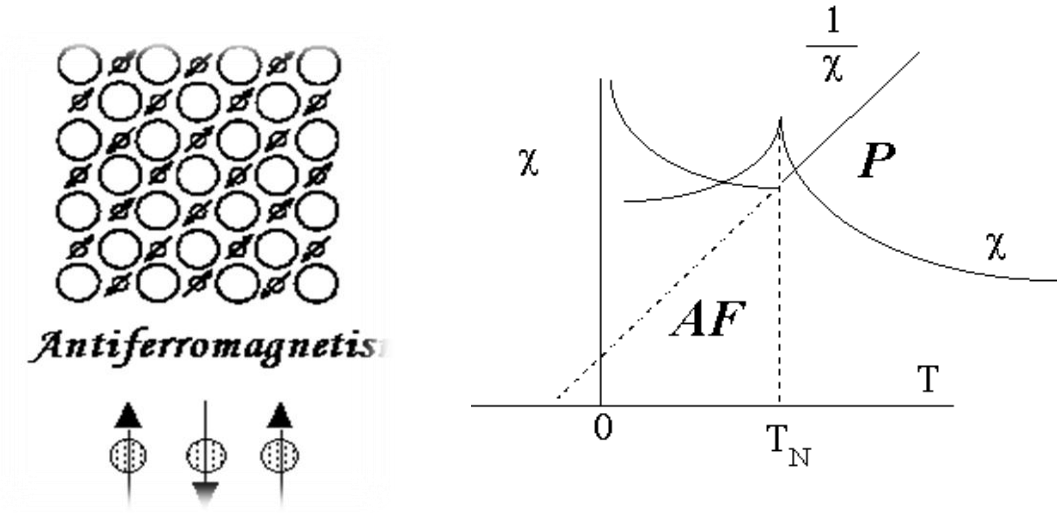

Figure 2.7: Domain alignment (left) and susceptibility as function of temperature (right) of antiferromagnetism.

The clue to antiferromagnetism (AF) is the behavior of susceptibility (χ) above a critical temperature, called the Néel temperature (T_N). Above T_N, the susceptibility obeys the Curie-Weiss law for paramagnets (P) but with a negative intercept indicating negative exchange interactions.

2.3 Nanomagnetism

Magnetic nanoparticles are being studied by a number of researchers owing to their potential applications in a variety of areas including magnetic devices, magnetic fluids, magnetic recording media, medical diagnosis, and hyperthermia [2-5] .One of the unique characteristics of magnetic nanoparticles is that the coercive force becomes zero at the superparamagnetic regime below a certain critical size because the random flipping of magnetization direction becomes dominant even at room temperature [6,7]. Based on the theory of magnetism, taking an ellipsoid for example, the total energy is contributed by three types of energies, exchange, anisotropy, and magnetostatic energy. With the increase in the size of a magnet, the number of domains will also increase. As a

result, there will be a decrease in the magnetostatic energy, while the more numerous domain walls will also raise the exchange and the anisotropy energies. Therefore, the size of the magnet has a great influence on its magnetic behavior, as can be illustrated by considering the coercivity of the magnet [8]. The size-dependent coercivity of magnets is shown schematically in Fig. 2.8.

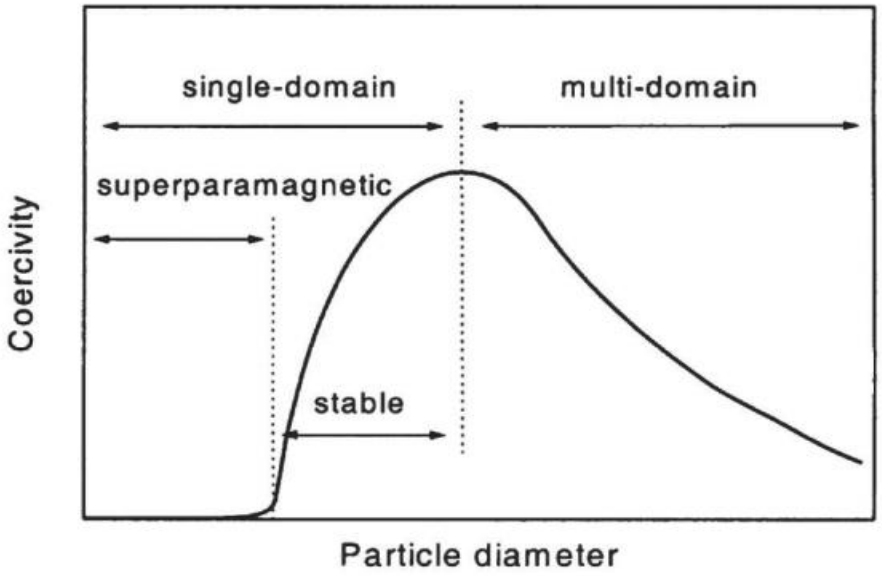

Figure 2.8: Size dependent coercivity of magnets.

First, for very small particles whose diameters are smaller than the critical diameter of superparamagnetism (D_{spm}), the magnetic moment is not stable. Secondly, in the range between D_{spm} and the critical diameter of a single domain (D_{sd}), the moment is stable, and the coercivity enlarges as D_{sd} increases. Finally, for larger diameters, the multi-domain region appears, and the coercivity declines with increasing particle diameter. Therefore, the magnet has the maximal coercivity when its diameter is equal to D_{sd}, and it will become superparamagnetic when its diameter becomes smaller than D_{spm}. In particular, for the single domain magnet, all the magnetic

moments are along the anisotropy axis, and the free energy contribution from exchange and anisotropy is zero.

2.3.1 Superparamagnetism

Superparamagnetism (SPM) is a type of magnetism that occurs in small ferromagnetic or ferrimagnetic nanoparticles. This implies sizes around a few nanometers to a couple of tenth of nanometers, depending on the material. Additionally, these nanoparticles are single-domain particles. In a simple approximation, the total magnetic moment of the nanoparticles can be regarded as one giant magnetic moment, composed of all the individual magnetic moments of the atoms which form the nanoparticle.

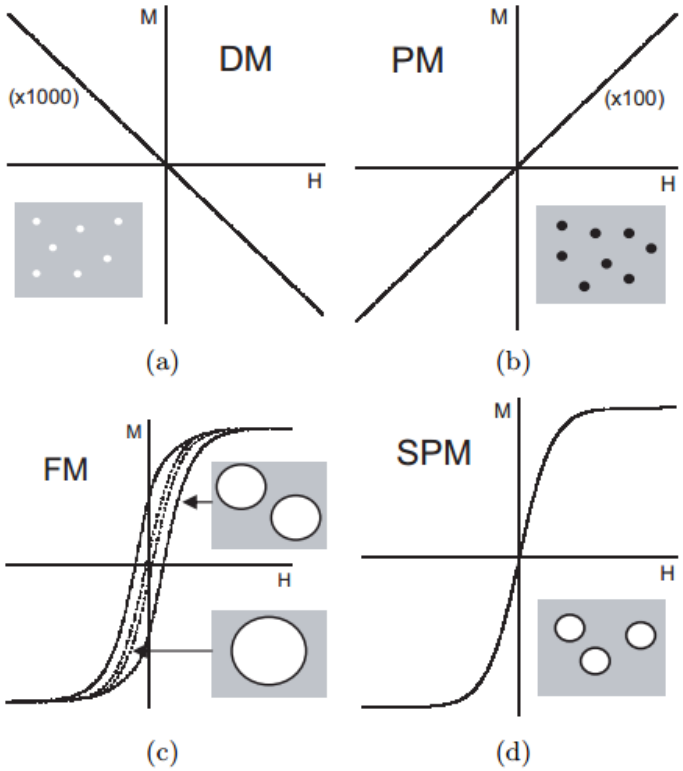

Figure 2.9: Schematic behavior of (a) Diamagnetic, (b) Paramagnetic, (c) Ferromagnetic, (d) Superparamagnetic materials in an external magnetic field.

2.4 Synthesis of Magnetic Nanostructures

Various approaches such as wet chemical [9-11], template-directed [12, 33], microemlusion [14-16], thermal decomposition [16, 17], solvo-thermal method [18, 19], solid state [20, 21], deposition method [22], spray pyrolysis [23, 24], self-assembly [25, 26], physical and lithographic [27, 28] techniques have been extensively used for the synthesis of a wide variety of magnetic nanostructures including iron oxide, metal, metal alloys and core–shell and composites structures. However a comprehensive review of various synthetic techniques is beyond the scope of this chapter, so here we will give a short description of only those methods that offer excellent size and shape control.

2.4.1 Chemical Synthesis

Several chemical methods that are being used for the synthesis of magnetic nanostructures comprise of co-precipitation, thermal decomposition, microemlusion and hydrothermal methods. Thermal decomposition and hydrothermal approaches provide better results (both in terms of size and morphology) in comparison with other synthetic routes [21]. Chemical syhthesis involved the precipitation of nano particles from the solution. To achieve the monodisperse particles, the precipitation should comply with the LaMer and Dinegar model of homogeneous precipitation. According to this model, during precipitation from the solution at certain stage of super saturation, there occur a burst of nucleation that gradually grows in size by diffusion of solutes from the solution towards the nuclei until the monodisperse final size particle are obtained. The mechanism LaMer and Dinegar model is shown in Figure 2.10.

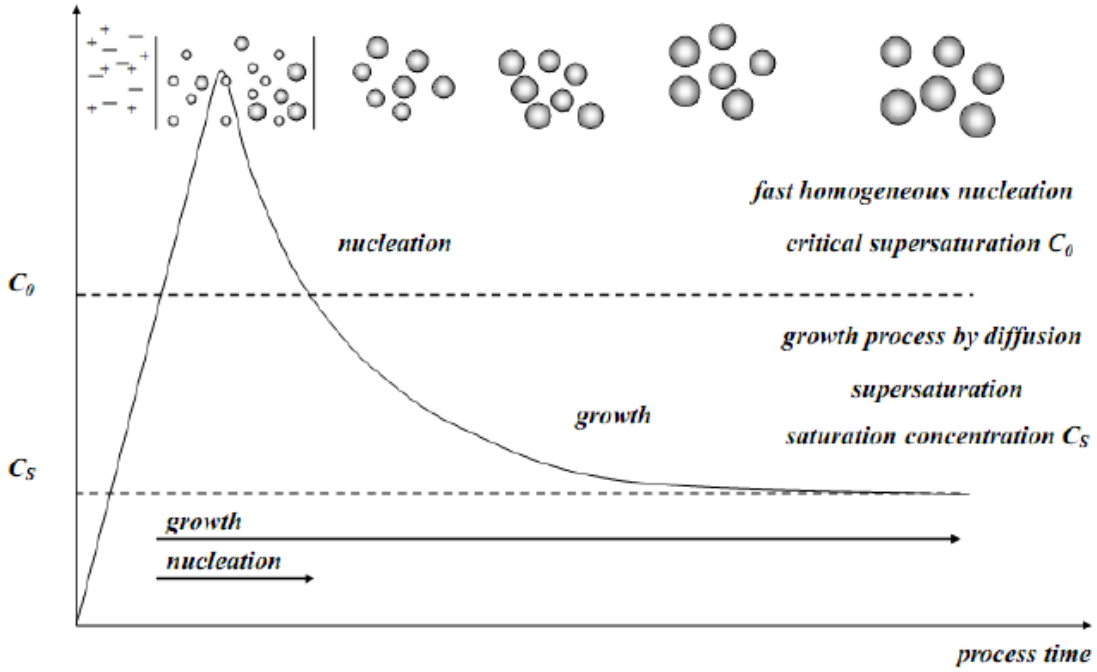

Figure 2.10: LaMer and Dinegar model.

2.4.1.1 Thermal Decomposition

This method of synthesis involves the chemical decomposition of the substance at elevated temperature. During this method the breaking of the chemical bond takes place. This method of synthesis for magnetic nanostructures mostly use organometallic compounds such as acetylacetonates in organic solvents (benzyl ether, Ethylenediamine and carbonyls) with surfactants such as oleic acid, oleylamine, polyvinyl pyrrolidone (PVP)**,** cetyltrimethyl ammonium bromide (CTAB) and hexadecylamine. In this method the composition of various precursors that are involved in the reaction determine the final size and morphology of the magnetic nanostructures. Peng *et al* and co-workers used the thermal decomposition approach for controlled synthesis (in term of size and shape) of magnetic oxide [29].

2.4.1.2 Hydrothermal Synthesis

Another important chemical synthesis technique that involves the use of liquid–solid–solution (LSS) reaction and gives excellent control over the size and shape of the magnetic nano particles is the hydrothermal synthesis. This method (figure 2.11) involves the synthesis of magnetic nano particles from high boiling point aqueous solution at high vapor pressure. It is a unique approach for the fabrication of metal, metal oxide [30, 31], rare earth transition metal magnetic nanocrystals [32], semi-conducting [33], dielectric, rare-earth fluorescent and polymeric [34]. This synthetic technique involved the fabrication of magnetic metallic nanocrystals at different reactions conditions. The reaction strategy is based upon the phase separation which occurs at the interface of solid–liquid–solution phases present in the reaction. For example the fabrication of monodisperse (6, 10 and 12 nm) Fe_3O_4 and MFe_2O_4 nanocrystals have been demonstrated by Sun *et al* and coworker [35].

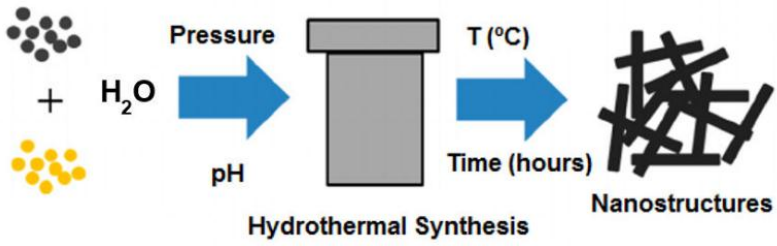

Figure 2.11: General steps of hydrothermal synthesis.

2.4.1.3 Sol-gel Synthesis

Sol–gel method is one of the well-established synthetic approaches to prepare novel NPs as well as nano-composites. This method has potential control over the textural and surface properties of the materials. Sol–gel method mainly undergoes in few steps to deliver the final metal oxide protocols and those are hydrolysis, condensation, and drying process. The formation of metal oxide involves different consecutive steps, initially the corresponding metal precursor undergoes rapid hydrolysis to produce the metal hydroxide solution, followed by immediate condensation which leads to the formation of three-dimensional gels. Afterward, obtained gel is subjected to drying

process, and the resulting product is readily converted to Xerogel or Aerogel based on the mode of drying. Sol–gel method can be classified into two routes, such as aqueous sol–gel and nonaqueous sol–gel method depending on the nature of the solvent utilized [36].

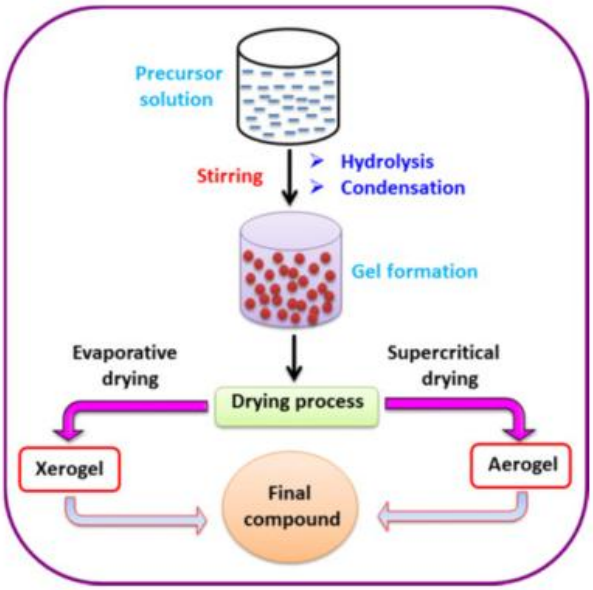

Figure 2.12: The reaction pathway for the production of nanostructures in the Sol–gel method.

2.4.2 Solid State Synthesis

Conventional mixed oxide method may also be named as solid state method. In solid state reaction method, individual oxides are mixed in stoichiometric quantities and are ground well to obtain homogeneous mixture. The grinding is made by different methods such as ball milling, mortar and pestle (ceramic) etc. The ground powder is subjected to annealing usually at elevated temperatures for longer time. This results in large particle size with wide particle size distribution. It also improves the compaction and thermal reactivity of powder by reducing particle size and creating defects inside the powder crystallites. The wet milling i.e. grinding in some alcoholic or aqueous medium is preferable than dry milling which adversely affects the particle size. Although this conventional process has become very old but it is still in practice to meet the massive demand of soft ferrite industry.

2.4.2.1 Ball Milling

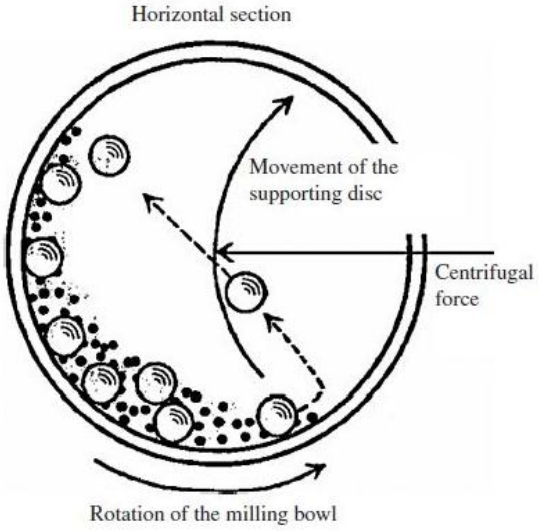

Figure 2.13: Schematic motion of the ball milling powder mixture.

A powder mixture placed in the ball mill is subjected to high-energy collision from the balls. This process was developed by Benjamin and his coworkers at the International Nickel Company in the late of 1960. A turn disc rotates in one direction while the bowls rotate in the opposite direction. The centrifugal forces, created by the rotation of the bowl around its own axis together with the rotation of the turn disc, are applied to the powder mixture and milling balls in the bowl. The powder mixture is fractured and cold welded under high energy impact. Magnetic nanoplates and nanoparticles are prepared by ball milling in the presence of surfactants in organic solvents [37].

2.4.2.2 Sonofragmentation

The utilization of ultrasonic energy in a process called sonofragmentation offers a facile, versatile synthetic tool for nanostructured materials that are often unavailable by conventional methods. Ultrasonic dispersion is extensively use to disperse sub-micron agglomerated powders in liquid suspensions. It is possible to break down the aggregates of nanocrystalline particles by using the multiple effects of ultrasound which generates many localized hot spots with the particles within the solution and during the process [38]. This topic has been further discussed in chapter 3.

References

[1] Coey J. M. D., *Magnetism and Magnetic Materials*. New York: Cambridge, ISBN-13 (2009) 978-0-511-67743-4.

[2] Willard M.A., Kurihara L.K., Carpenter E.E., Calvin S., Harris V.G., Chemically prepared magnetic nanoparticles. *Inter. Mater. Rev*., 49 (2004), 125–170.

[3] Sun S., Murray C.B., Weller D., Folks L., Moser A., Monodisperse FePt Nanoparticles and Ferromagnetic FePt Nanocrystal Superlattices. *Science*, 287 (2000), 1989–1992.

[4] Li C., Ma C., Wang F., Xil Z., Wang Z., Deng Y., He N., Preparation and biomedical applications of core-shell silica/magnetic nanoparticle composites. *J. Nanosci. Nanotechnol*., 12 (2012), 2964–2972.

[5] Mou X., Ali Z., Li S., He N., Applications of magnetic nanoparticles in targeted drug delivery system. *J. Nanosci. Nanotech*., 15 (2015), 54–62.

[6] Krishnan K.M., Pakhomov A.B., Bao Y., Blomqvist P., Chun Y., Gonzales M., Griffin K., Ji, X., Roberts B.K., Nanomagnetism and spin electronics: materials, microstructure and novel properties. *J. Mater. Sci*., 41 (2006), 793–815.

[7] Lim C.W., Lee I.S., Magnetically recyclable nanocatalyst systems for the organic reactions. *Nano Today* 5 (2010), 412–434.

[8] Guimar P., *Principles of Nanomagnetism*. Berlin: SpringerVerlag, 2009.

[9] Sun J., Synthesis and characterization of biocompatible Fe_3O_4 nanoparticles. *Journal of Biomedical Materials Research Part A*, 80 (2007), 333-341.

[10] Liu Z., Single crystalline magnetite nanotubes. *Journal of the American Chemical Society*, 127 (2005), 6-7.

[11] Zhong Z., A versatile wet-chemical method for synthesis of one-dimensional ferric and other transition metal oxides. *Chemistry of materials*, 18 (2006), 6031-6036.

[12] Jiao F., Synthesis of ordered mesoporous Fe_3O_4 and γ-Fe_2O_3 with crystalline walls using post-template reduction/oxidation. *Journal of the American Chemical Society*, 128 (2006), 12905-12909.

[13] Du N., Selective synthesis of Fe_2O_3 and Fe_3O_4 nanowires via a single precursor: a general method for metal oxide nanowires. *Nanoscale research letters*, 5 (2010), 1295-1300.

[14] Wang G., The synthesis of magnetic and fluorescent bi-functional silica composite nanoparticles via reverse microemulsion method. *Journal of fluorescence*, 19 (2009), 939-946.

[15] Jin J., Ohkoshi S.I., Hashimoto K., Giant coercive field of nanometer-sized iron oxide. *Advanced Materials*, 16 (2004), 48-51.

[16] Han Y.C., Synthesis of highly magnetized iron nanoparticles by a solvent less thermal decomposition method. *The Journal of Physical Chemistry C*, 111 (2007), 6275-6280.

[17] Sun S., Zeng H., Size-controlled synthesis of magnetite nanoparticles. *Journal of the American Chemical Society*, 124 (2002), 8204-8205.

[18] Kang M., Synthesis of Fe/TiO photocatalyst with nanometer size by solvo-thermal method and the effect of HO addition on structural stability and photodecomposition of methanol. *Journal of Molecular Catalysis A: Chemical*, 197 (2003), 173-183.

[19] Ai L., Zhang C., Chen Z., Removal of methylene blue from aqueous solution by a solvothermal-synthesized graphene/magnetite composite. *Journal of hazardous materials*, 192 (2011), 1515-1524.

[20] Park J., Ultra-large-scale syntheses of monodisperse nanocrystals. *Nature Materials*, 3 (2004), 891-895.

[21] Teja A.S., Koh P.Y., Synthesis, properties, and applications of magnetic iron oxide nanoparticles. *Progress in Crystal Growth and Characterization of Materials*, 55 (2009), 22-45.

[22] Guo Q., Patterned Langmuir-Blodgett films of monodisperse nanoparticles of iron oxide using soft lithography. *Journal of the American Chemical Society*, 125 (2003), 630-631.

[23] Taniguchi I., Powder properties of partially substituted $LiM_xMn_2O_4$ (M= Al, Cr, Fe and Co) synthesized by ultrasonic spray pyrolysis. *Materials Chemistry and Physics*, 92 (2005), 172-179.

[24] Dosev D., Magnetic/luminescent core/shell particles synthesized by spray pyrolysis and their application in immunoassays with internal standard. *Nanotechnology*, 18 (2007), 055102.

[25] Zhong L.S., Self-Assembled 3D flowerlike iron oxide nanostructures and their application in water treatment. *Advanced Materials*, 18 (2006), 2426-2431.

[26] Polshettiwar V., Baruwati B., Varma R.S., Self-assembly of metal oxides into three-dimensional nanostructures: synthesis and application in catalysis. *ACS Nano*, 3 (2009), 728-736.

[27] Jia, C. J., Large-scale synthesis of single-crystalline iron oxide magnetic nanorings. *Journal of the American Chemical Society*, 130 (2005), 16968-16977.

[28] Li Z., One-Pot Reaction to Synthesize Biocompatible Magnetite Nanoparticles. *Advanced Materials*, 17 (2005), 1001-1005.

[29] Jana N.R., Chen Y., Peng X., Size-and shape-controlled magnetic (Cr, Mn, Fe, Co, Ni) oxide nanocrystals via a simple and general approach. *Chemistry of Materials*, 16 (2004), 3931-3935.

[30] Adschiri, T., Hydrothermal synthesis of metal oxide nanoparticles at supercritical conditions. *Journal of Nanoparticle Research*, 3 (2001), 227-235.

[31] Yu J., Yu X., Hydrothermal synthesis and photocatalytic activity of zinc oxide hollow spheres. *Environmental science & technology*, 42 (2008), 4902-4907.

[32] Yang T., Room-temperature ferromagnetic Mn-doped ZnO nanocrystal synthesized by hydrothermal method under high magnetic field. *Materials Science and Engineering*: B, 170 (2010), 129-132.

[33] Hu J., Bando Y., Growth and optical properties of single-crystal tubular ZnO whiskers. *Applied Physics Letters*, 82 (2003), 1401-1403.

[34] Wang X., A general strategy for nanocrystal synthesis. *Nature*, 437 (2005), 121-124.

[35] Sun S., Monodisperse MFe_2O_4 (M= Fe, Co, Mn) nanoparticles. Journal of the *American Chemical Society*, 126 (2004), 273-279.

[36] Bolla G. R., Benjaram M. R., Novel approaches for preparation of nanoparticles, *Nanostructures for Novel Therapy* (2017), www.sciencedirect.com/topics/chemistry/sol-gel-process.

[37] Poudyal N., Chuan-bing R. Ping Liu J., Morphological and magnetic characterization of Fe, Co, and FeCo nanoplates and nanoparticles prepared by surfactants-assisted ball milling. *Journal of Applied Physics* 109 (2011), 07B526.

[38] Basith M. A., Ngo D. T., Quader A., Rahman M. A., Sinha B. L., Ahmmad B., Simple top-down preparation of magnetic $Bi_{0.9}Gd_{0.1}Fe_{1-x}Ti_xO_3$ nanoparticles by ultrasonication of multiferroic bulk material, Nanoscale 6 (2014), 23, 14336-14342.

CHAPTER 3

SAMPLE PREPARATION

3.1 Introduction

In this chapter, experimental methods of sample preparation techniques are discussed. A brief description of the apparatus used are also given. Basic techniques of sample preparation and experimental techniques are illustrated in this chapter.

3.2 Materials and method

The precursor materials of Fe, Ni and Co powder were purchased from Merck KGaA, Germany. 2-isopropanol of analytical grade was also purchased from Merck KGaA, Germany and used without further purification. Deionized water was used in all the experiments. In a typical synthesis, weighing Fe and Ni/Co powder in stoichiometric proportion and then mixed together for homogeneous mixture. After that, the mixture was thoroughly grounded by performing manual grinding for approximately three hours. The obtained mixture powder was further mixed with 2-isopropanol with a ratio of 40 mg powder and 10 ml isopropanol with a mass percentage of ~ 0.25%. Then the mixtures of isopropanol and powder were put into ultrasonication bath for 30 minutes. After this, the precipitant was collected and used for the investigation of structural and magnetic properties.

After six hours, the precipitant was used for the investigation of structural and magnetic properties.

Figure 3.1: Sample preparation method.

3.2.1 Ultrasonication Technique

In ultrasonication technique, the ultrasonic wave energy is used to synthesis nanoparticles that disperse the agglomerated materials into single particle. Details mechanism of the ultrasonication technique are given below.

This brief overview highlights the basic aspects of ultrasonic generation and propagation relevant to particle dispersion [1]. During the process of ultrasonic disruption, sound waves propagate through the liquid medium in alternating high and low pressure cycles at frequencies typically in the 20-40 kHz range. During the low-pressure cycle (rarefaction), microscopic vapor bubbles are formed in a process known as cavitation (figure 3.2). The bubbles then collapse during the high

pressure cycle (compression) producing a localized shock wave that releases tremendous mechanical and thermal energy.

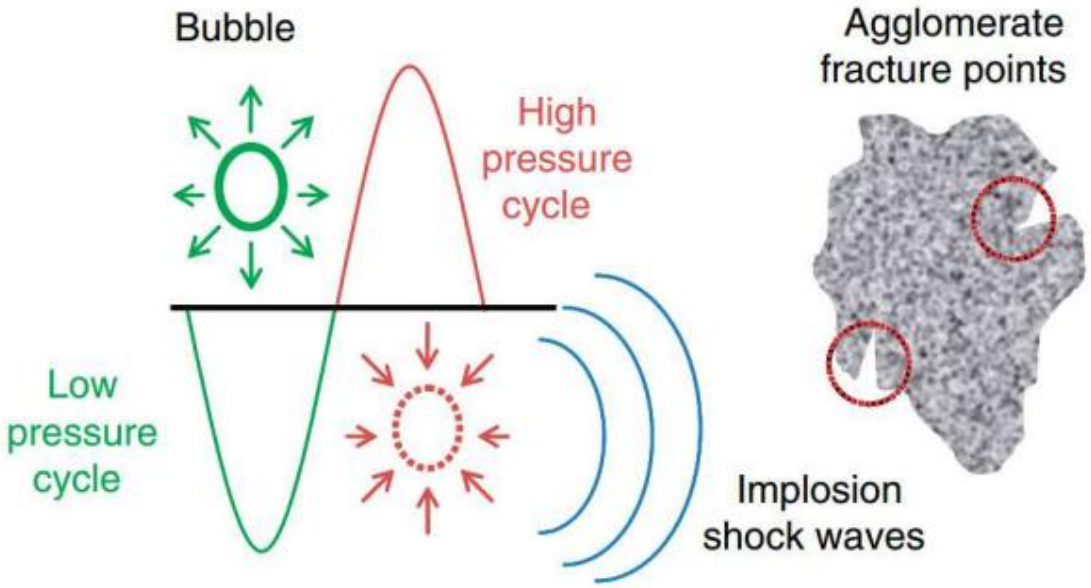

Figure 3.2: Schematic illustration of ultrasonic wave-induced cavitation and agglomerate fracture.

Ultrasonic waves can be generated in a liquid suspension either by immersing an ultrasound probe (transducer horn) into the suspension (direct sonication), or by introducing the sample container into a liquid that is propagating ultrasonic waves (indirect sonication). This is shown schematically in figure 3.3.

In a sonication bath or a so-called cup horn sonicator (indirect sonication), the sound waves must travel through both the bath or cup liquid (typically water) and the wall of the sample container before reaching the suspension. In direct sonication, the probe is in contact with the suspension, reducing the physical barriers to wave propagation and therefore delivering a higher effective

energy output into the suspension. Bath sonicators typically operate at much lower energy levels than are attainable using a probe or cup horn. In the case of bath sonicators, the transducer element is directly attached to the outside surface of the metal tank, and the ultrasonic waves are transmitted directly to the tank surface and then into the bath liquid. In a cup horn, the radiating surface of the horn is inverted and sealed into the bottom of a (typically) transparent plastic cup into which the sample container is immersed.

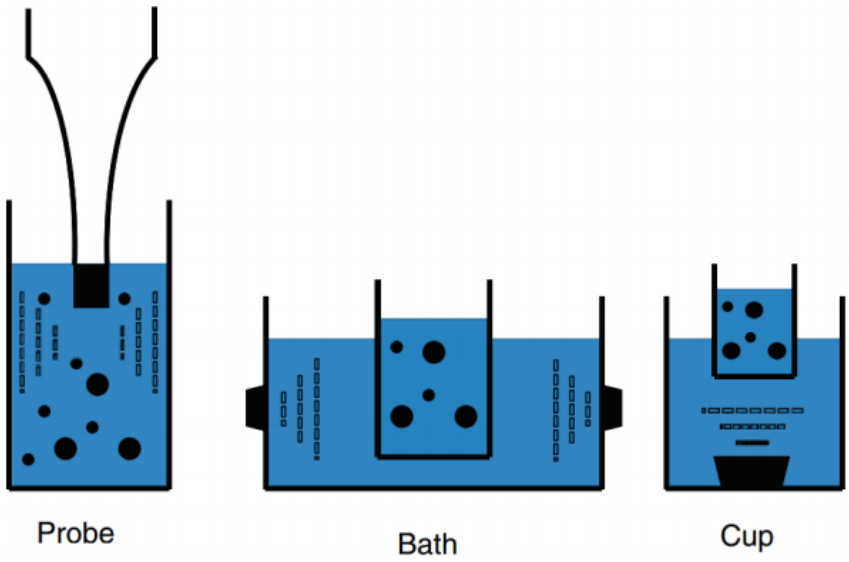

Figure 3.3: Schematic illustration of direct (left) and indirect (middle and right) sonication configurations as described in the text.

At ultrasound frequencies, the alternating formation, growth and subsequent shock waves produced by the collapse of bubbles result in extremely large (localized temperatures up to 10000 K, rapid temperature changes ($> 10^5$ Ks^{-1}), pressure bursts on the order of several MPa, and liquid jet streams with speeds reaching 400 kmh^{-1}). Such massive, local energy output is the basis of the disruptive effect of sonication. It must be noted that these considerable pressure and temperature differentials are a result of the cavitation process and occur at the local interface of the exploding

bubbles; consequently, these effects are inherent to the sonication process and will occur whether the sonicated container is cooled or not, or the treatment performed using a bath, cup horn, or a probe sonicator.

In all cases, the ultrasonic device transforms electrical power into vibrational energy by means of a piezoelectric transducer that changes its dimensions in response to an applied AC electric field. A sonicators stated maximum power (e.g., 600 W) refers to the maximum theoretical power it would be able to consume, should it require so; it does not reflect the actual amount of ultrasonic energy delivered to the suspension. That is, for the same frequency and amplitude (and thus the same sonicator setting), the sonicator would need to consume more power to treat a high viscosity suspension than it would for a low viscosity suspension, and if so, it could consume up to a maximum of 600 W. It is therefore erroneous to assume that selecting the highest setting value will result in the delivery of the instruments nominal maximum power to the sonicated suspension. For low viscosity media, even at the highest setting value, the delivered power will be a significantly lower fraction of the instruments maximum power rating. Similarly, the power value (measured in W) usually shown on the instrument display reflects the power that the instrument is consuming from the electrical source to produce the desired oscillation amplitude (from the selected setting value) in the sonicated medium. The consumed (i.e., displayed) power, however, does not necessarily reflect the power that is actually delivered to the sonicated suspension. Herein lies the deficiency with reporting either the manufacturers stated maximum power, the adjustable output power reading provided by the instrument, or the chosen setting level. The net fragmentation effect from applying ultrasonic energy to a suspension is dependent on the total amount of energy delivered to the sonicated medium. However, not all of the produced cavitational energy is effectively utilized in disrupting particle clusters. The delivered energy is consumed or

dissipated by several mechanisms, including thermal losses, ultrasonic degassing, and chemical reactions, such as the formation of radical species. Only a portion of the delivered energy is actually used in breaking particle-particle bonds to produce smaller particle aggregates, agglomerates, and primary particles. Moreover, an excessive energy input can potentially result in agglomerate formation or re-agglomeration of previously fragmented clusters, as well as induce a variety of physicochemical alterations on the materials surface or to the constituents of the suspending medium. Such sonication-specific side-effects are addressed in the following sections, but first we examine the particle disruption process as it is the primary objective of ultrasonic treatment.

3.2.2 Sonication Effects on Particle Disruption and Aggregation

The properties of synthesized nanoparticles are strongly dependent on the particle size of the processed material. For instance, the size of the particles in suspension dictates along with the particles surface chemistry and their photocatalytic activity and arsenic removal from water. Additionally, the agglomeration state determines whether the particles will settle out or remain in suspension, which directly impacts in magnetization, polarization and leakage current [2]. Numerous other examples of size-dependent behavior can be found in the recent literature.

Dry powders consist of particles that are bound together into macroscopic structures by both weak physical Vander Waals forces and stronger chemical bonds including particle fusion. Commonly, these powders contain micro meter and submicrometer scale aggregates, which are in turn held together by physical forces to constitute larger agglomerates. This is depicted schematically in figure 3.4. For powders consisting of nanoscale particles and aggregates, and therefore having substantial interfacial contact areas per unit volume, the nominally Vander Waals forces can be

extremely large, requiring the use of techniques such as sonication to effectively break down or disrupt powder agglomerates. In contrast, micro meter size primary particles can often be dispersed with moderate mixing or stirring.

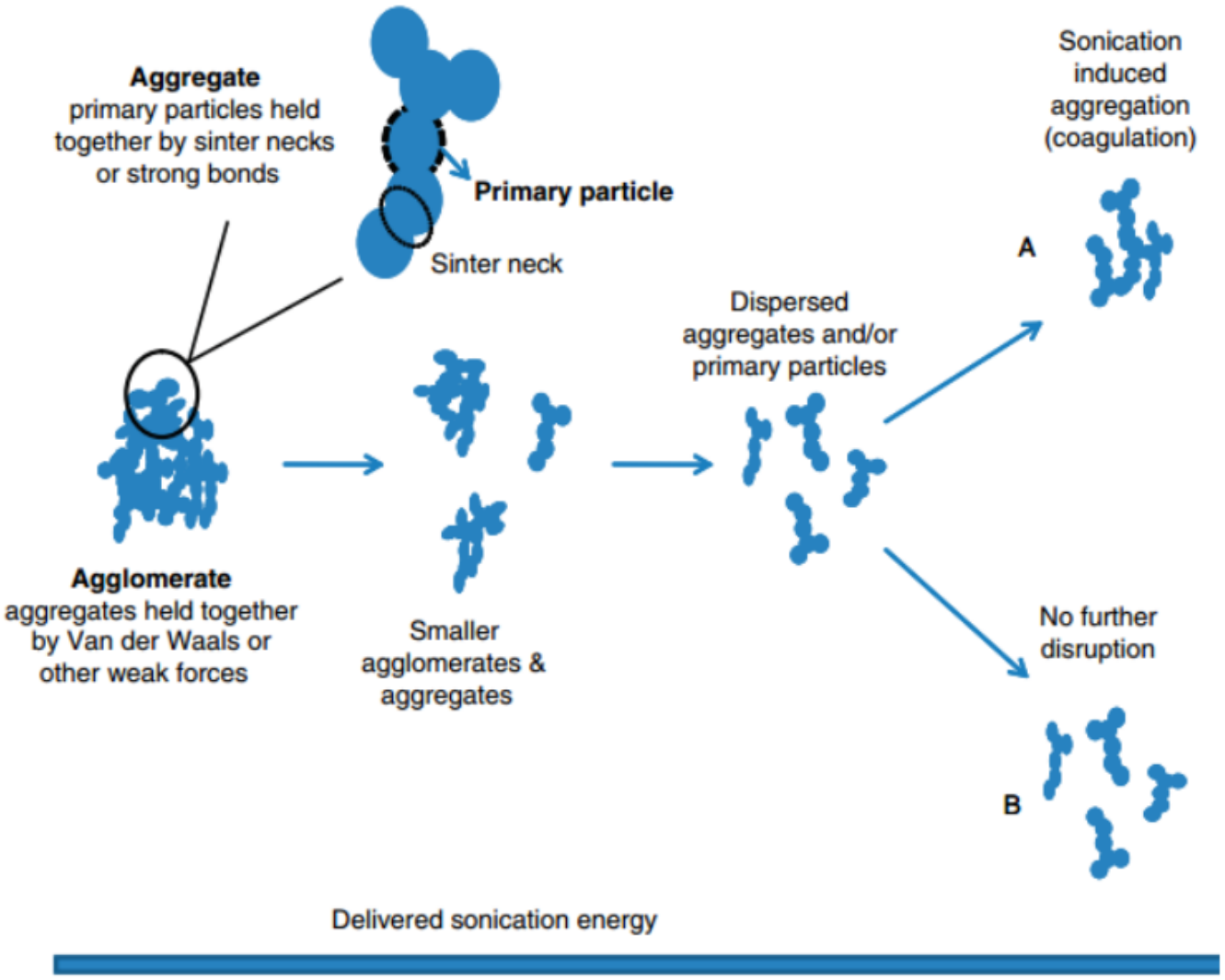

Figure 3.4: Schematic depiction of particle structures referred to in the text, and illustration of the typical effects of sonication on particle size as a function of delivered sonication energy.

References

[1] Julian S., Taurozzi, Vincent A., Hackley, Mark R., Wiesner, Ultrasonic dispersion of nanoparticles for environmental, health and safety assessment issues and recommendations, *Nanotoxicology,* 5 (2011): 711729.

[2] Mehedi H, Hakim M. A., Basith M. A., Sarowar M, Bashir A, Zubair M. A., Hussain A., Fakhrul M. I., Size dependent magnetic and electrical properties of Ba-doped nanocrystalline $BiFeO_3$, *AIP Advances* 6 (2016), 035314.

CHAPTER 4

EXPERIMENTAL TECHNIQUES

4.1 Introduction

This chapter presents characterization and experimental techniques used in this thesis. X-ray Diffraction was used to determine the crystal structure and lattice parameters. Surface morphology and microstructure measurements were carried out by Scanning Electron Microscopy. Elemental analysis was done by Energy Dispersive spectroscopy (EDS). DC magnetization measurements were carried out using Vibrating Sample Magnetometer.

4.2 X-ray Diffraction

One of the most fundamental studies used to characterize the structure of materials is X-ray diffraction. This technique uses the principle that waves interacting with atomic planes in a material will exhibit the phenomenon of diffraction. X-rays incident on a sample are scattered off at an equal angle. At certain angles of incidence, X-rays scattering off from neighboring parallel planes of atoms will interfere destructively. At other angles, these waves will interfere constructively and result in a large output signal at those angles. The XRD technique is based on Bragg's principle. Bragg reflection is a coherent elastic scattering in which the energy of the X-ray is not changed on reflection. If a beam of monochromatic radiation of wavelength λ is incident on a periodic crystal plane at an angle θ and is diffracted at the same angle as shown in Figure 4. 1, the Bragg diffraction condition for X –rays is given by

$$2d \sin\theta = n\lambda \quad (4.1)$$

where d is the distance between crystal planes and n is the positive integer which represents the order of reflection. Equation (4.1) is known as Bragg law. This Bragg law suggests that the diffraction is only possible when $\lambda \leq 2d$ [1]. For this reason we cannot use the visible light to determine the crystal structure of a material.

The lattice parameter for each peak of each sample was calculated by using the formula. (for cubic spinel structure)

$$a = d\sqrt{(h^2 + k^2 + l^2)} \quad (4.2)$$

Where h, k and l are the Miller indices [1] of the crystal planes. Various properties of any crystal structure like inter-planner distance, lattice parameters etc. can be measured by X-ray diffraction (XRD).

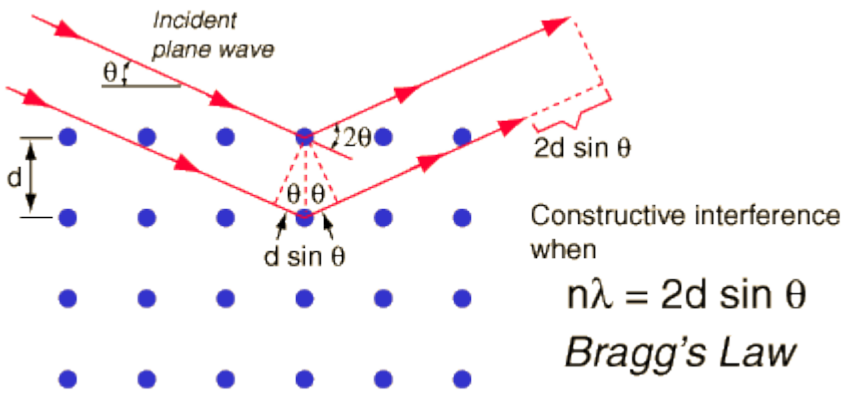

Figure 4.1: Bragg's law of X-ray diffraction.

To determine exact lattice parameter for each sample, Nelson-Riley [2] method was used. The Nelson-Riley function F (θ) is given as

$$F(\theta) = \frac{1}{2}\left[\frac{cos^2}{\sin\theta} + \frac{cos^2}{\theta}\right] \quad (4.3)$$

The values of lattice parameter 'a' of all the peaks for a sample are plotted against F(θ). Then using a least square fit method, exact lattice parameter 'a_o' is determined. The point where the least square fit straight line cut the y-axis (i.e. at F (θ) = 0) is the exact lattice parameter of the sample.

4.2.1 Crystallite Size Measurement

Particle size determination is important in the ferromagnetic nanoparticles. In case of fine particles, with reduction in the size of the particles, the XRD lines get broadened, which indicates clearly that particle size has been reduced. Information of the particle size is obtained from the full width at half maximum (FWHM) of the diffraction peaks. A crystal is usually considered perfect when atoms occupy all lattice sites and no imperfection exists in the crystal. The broadening of diffraction peaks arises mainly due to three factors. The peaks become broader due to the effect of small crystallite sizes and thus an analysis of peaks broadening can be used to determine the crystallite sizes introduce additional broadening into the diffraction peaks.

The condition for constructive interference, reinforcement of X-ray scattering from a crystalline powder is given by Bragg's law which is given by $2d \sin\theta = n\lambda$. This equates the path difference of X-ray scattered from parallel crystalline planes spaced $d = d_{hkl}$ apart to an integral (n) number of X-ray wavelength, λ. Here θ is the diffraction angle measured with respect to the crystalline planes. For an infinite crystal Bragg scattering occurs at discrete values of 2θ

satisfying the Bragg condition, i.e. Bragg peaks are δ-function. For finite sized crystals the peaks are broadened over a range of angle.

To understand the phenomenon of fine particle broadening, we consider a finite crystal of thickness, D = md, where m is an integer and d is the distance between crystal planes, i.e. there are m planes in D.

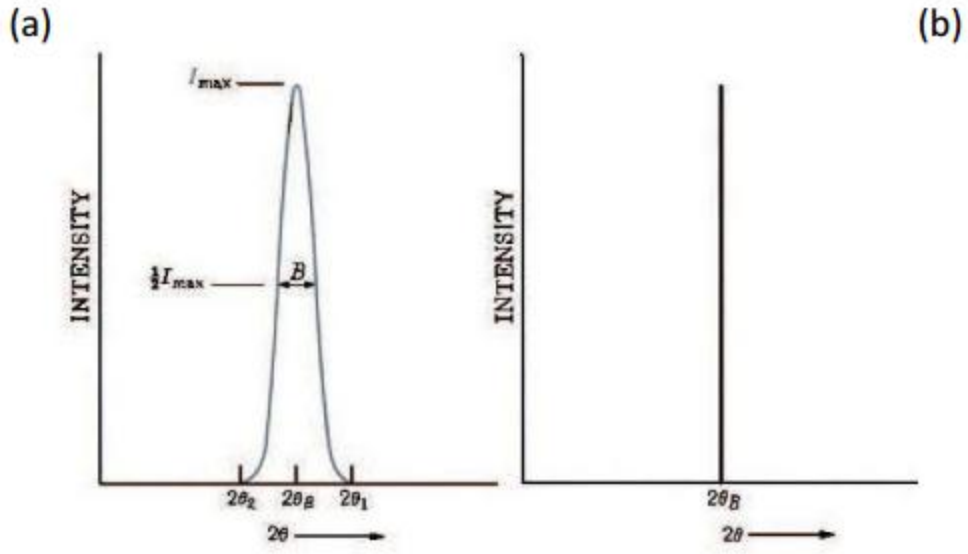

Figure 4.2: Effect of fine particle size on diffraction curves (Schematic):

(a) small particle size and (b) large particle size.

Considering Figure 4.2, if the broadened Bragg peak begins at an angle $2\theta_2$ and ends at $2\theta_1$, the breadth of the peaks or full width at half maximum (FWHM) is given as

$$\beta = \frac{1}{2}(2\theta_1 - 2\theta_2) = \theta_1 - \theta_2$$

Now if we consider the path differences for each of the two angles θ_1 and θ_2 for Xray traveling the full thickness of the crystal. The width β is usually measured in radians. We now write path difference equations for these two angles, related to the entire thickness of the crystal rather to the distance between adjacent planes

$$2D \sin\theta 1 = (m+1)\lambda$$

$$2D \sin\theta 2 = (m-1)\lambda$$

By subtracting we find $D(\sin\theta 1 - \sin\theta 2) = \lambda$

$$2D \cos\left(\frac{\theta 1+\theta 2}{2}\right) \sin\left(\frac{\theta 1-\theta 2}{2}\right) = \lambda$$

As $\theta 1$ and $\theta 2$ are nearly equal to θ, so $\theta 1 + \theta 2 \approx 2\theta$ and $\sin\left(\frac{\theta 1-\theta 2}{2}\right) \approx \left(\frac{\theta 1-\theta 2}{2}\right)$. Thus the above equation can be written as,

$$2D \cos\left(\frac{2\theta}{2}\right)\left(\frac{\theta 1-\theta 2}{2}\right) = \lambda$$

From above we get,

$$D = \frac{\lambda}{\beta \cos\theta}$$

A more exact empirical treatment yields:

$$D_{xrd} = \frac{0.9\,\lambda}{\beta \cos\theta}$$

This is known as the Scherrer's formula. It is used to estimate the particle size of very small crystal from the measured width of their diffraction curves.

4.3 Surface Morphology and Microstructure

The microstructural study was performed in order to have an insight of the grain structures. The samples of different compositions and sintered at different temperatures were chosen for this purpose. The samples were visualized under a high-resolution Scanning Electron Microscope (SEM) and then photographed. Average grain sizes (grain diameter) of the samples were determined from SEM micrographs by linear intercept technique [3]. To do this, several random horizontal and vertical lines were drawn on the micrographs. Therefore, we counted the number of grains intersected and measured the length of the grains along the line traversed. Finally the average grain size was calculated.

4.3.1 Scanning Electron Microscope (SEM)

The SEM is the most routinely utilized instruments for the characterization of micro/nanomaterials. Using SEM it is possible to obtain secondary electron images of metallic particles with nanoscale resolution, allowing topographical and morphological studies can be carried out. In sensor technology, this is predominantly used to study surfaces of thin films and sensing layers [4]. A schematic diagram of an SEM is shown in fig.4.3. The electron beam is emitted from a heated filament, which is commonly made from lanthanum hexaboride (LaB_6) or tungsten. The filament is heated by applying a voltage, which causes electrons to be emitted. Alternatively, electrons can be emitted via field emission (FE). The electrons are accelerated towards the sample by applying an electric potential. This resulting electron beam is focused by a condenser lens, which projects the image of the source onto the condenser aperture. It is then

focused by an objective lens and raster-scanned over the sample by scanning coils. This is achieved by varying the voltage produced by the scan generator on the scan coils that are energized, creating a magnetic field, which deflects the beam back and forth in a controlled pattern.

When the primary electrons hit the sample, they give part of their energy to electrons in the sample, resulting in the emission of secondary electrons. These secondary electrons have lower energies (around 20 eV). These secondary electrons are collected by an Everhart-Thornley detector, converted to a voltage, amplified and build the image. Their intensity is displayed versus the position of the primary beam on the sample.

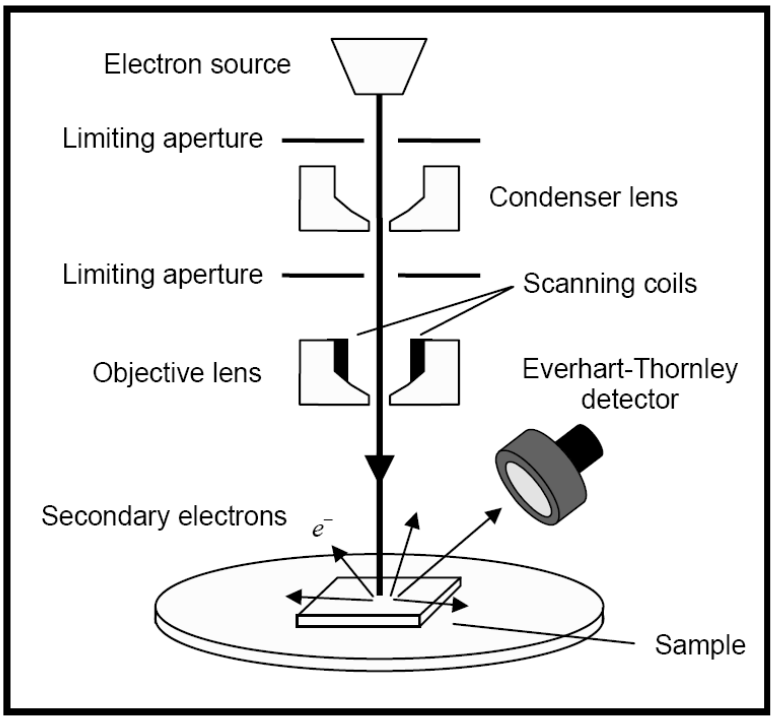

Figure 4.3: Schematic diagram of SEM setup [5].

The samples placed in the SEM must be either conducting or covered with a thin metal layer in order to avoid electric charging. Scanning takes place at low pressures, so that the electrons are not scattered by gas molecules inside the chamber [6]. Furthermore, with an SEM it is possible to

obtain images from comparatively large area of the sample. In addition to secondary electrons there are also high-energy electrons, originating in the electron beam (producing X-rays), that are backscattered from the specimen interaction volume. These electrons may be used to detect contrast between areas with different chemical compositions.

Also, SEM can monitor the formation and growth of thin films and nanostructures. In nanotechnology enabled sensing applications, the SEM plays a vital role in helping researchers understand the interaction between the sensing layer/media and the analyte. This is because sensitivity is strongly dependent on surface morphology and topography. Nowadays SEMs are designed for specific purposes ranging from routine morphological studies, cryogenic studies, to high-speed compositional analyses or for the study of environment-sensitive materials.

Figure 4.4: Scanning Electron Microscopy. (SEM).

4.3.2 Scanning Process and Image Formation

In a typical SEM, an electron beam is thermionically emitted from an electron gun fitted with a tungsten filament cathode. Tungsten is normally used in thermo ionic electron guns because it has the highest melting point and lowest vapor pressure of all metals, thereby allowing it to be heated for electron emission, and because of its low cost. The electron beam, which typically has an energy ranging from a few 100 eV to 40,000 eV, is focused by one or two condenser lenses to a spot about 0.4 nm to 5 nm in diameter. The beam passes through pairs of scanning coils or pairs of deflector plates in the electron column, typically in the final lens, which deflect the beam in the x and y axes so that it scans in a raster fashion over a rectangular area of the sample surface.

When the primary electron beam interacts with the sample, the electrons lose energy by repeated random scattering and absorption within a teardrop-shaped volume of the specimen known as the interaction volume, which extends from less than 100 nm to around 5 μm into the surface. The size of the interaction volume depends on the electron's landing energy, the atomic number of the specimen and the specimen's density. The energy exchange between the electron beam and the sample results in the reflection of high-energy electrons by elastic scattering, emission of secondary electrons by inelastic scattering and the emission of electromagnetic radiation, each of which can be detected by specialized detectors. The beam current absorbed by the specimen can also be detected and used to create images of the distribution of specimen current. Electronic amplifiers of various types are used to amplify the signals which are displayed as variations in brightness on a cathode ray tube. The raster scanning of the CRT display is synchronized with that of the beam on the specimen in the microscope, and the resulting image is therefore a distribution map of the intensity of the signal being emitted from the scanned area of the specimen. The image

may be captured by photography from a high resolution cathode ray tube, but in modern machines is digitally captured and displayed on a computer monitor.

4.4 Energy Dispersive Analysis by X-rays

We have used the energy dispersive analysis for determining the composition of magnetic labels. The EDAX measurement is a plot between intensity and X-ray energy of different elements. As the X-rays are characteristics of a material, by looking at the intensity for a particular energy the concentration of an element in a given material can be determined. In the following, the principle and operation of EDAX are discussed. The foundation for EDX analysis to determine composition was laid by Mosley who observed that the frequency of X-rays from different elemental targets varied in a linear way with atomic number. When any material is struck by electron beam or other charged particles such as proton or alpha particles or by photons such as X-rays or γ-rays, then atoms of the material get excited. The interaction of the beams with the materials depends on the energy of the beams [7-8].

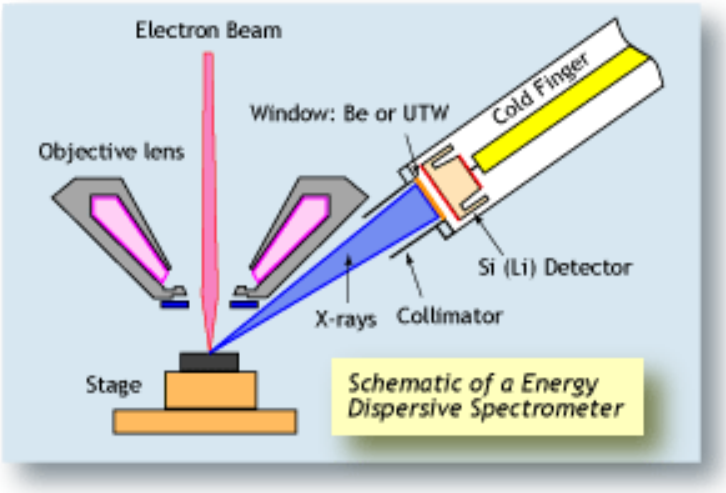

Figure 4.5: Schematic representation of EDS Instrument.

4.5 Magnetization Measurement

The vibrating sample magnetometer (VSM) measuring the magnetic properties of materials was first developed by S. Foner in 1956 and has been accepted as a standard approach worldwide as it has been the most successful for low temperature and high magnetic field studies of correlated electron system due to its simplicity, ruggedness, ease of measurement, and relatively high sensitivity. The working principle of VSM is based on Faraday's law of electromagnetic induction. In a VSM, a sample is attached to a vibrating rod and allowed to vibrate in a magnetic field produced by electromagnets. As the magnetization of the samples increases due to the increasing magnitude of the field, the change in flux induces a resulting in a voltage signal measured by induction coils located near the samples. The signal is usually small, and is measured by a lock-in amplifier at a frequency specified by the signal from the sample vibrator.

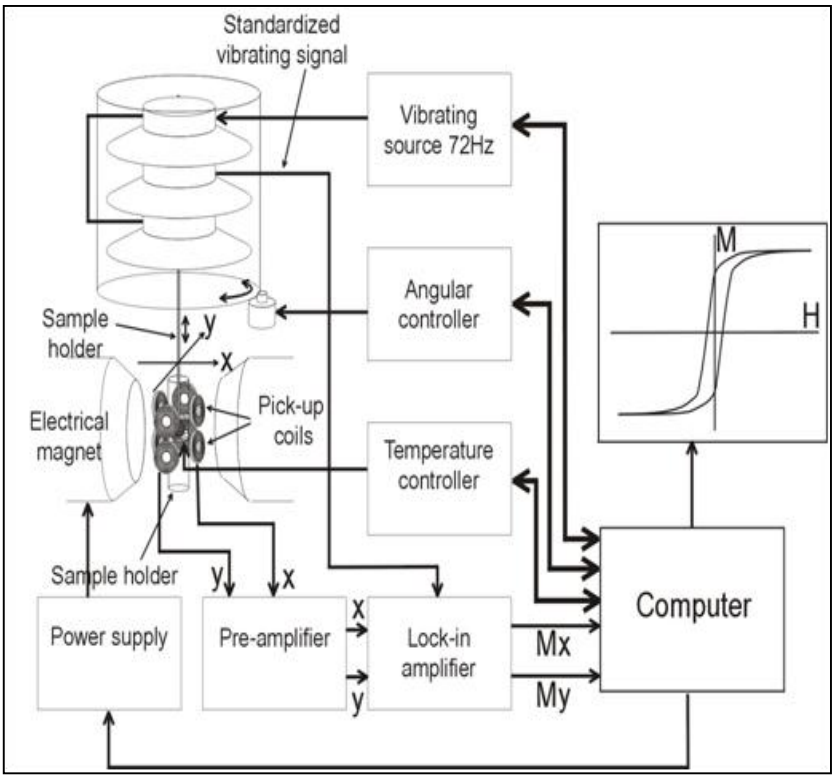

Figure 4.6: Block diagram of VSM.

The signal measured by the induction coil is directly proportional to the magnetization of the sample, and independent of the external field intensity. Plotting the induction *vs.* magnetic field intensity (H) results in a hysteresis curve representative of the stabilize magnetic moment although it can lack adequate sensitivity on ultra-thin films or samples with only small amounts of the magnetic moment. The measurements of this report were done using Lakeshore 7400 series VSM. The schematic block diagram of the VSM is shown in Figure 4.6 along with a VSM machine in Figure 4.7.

Figure 4.7: Vibrating Sample Magnetometer (VSM)

References

[1] Kittel C., *Introduction to Solid State Physics*, 7th edition, John Wiley & Sons, Inc., Singapore, 1996.

[2] Nelson J.B., Riley D.P., *Cavendish laboratory*, Cambridge, 1944.

[3] Hossain A.K.M.A., "*Investigation of colossal magnetoresistance in bulk and thick film magnetites*", *Ph. D. Thesis*, Imperial College, London, 1998.

[4] Butt H. J., Graf K., and Kappl M., "*Physics and chemistry of interfaces*", (Wiley-VCH, Weinheim, Germany, 2003)

[5] Kourosh Kalntar-Z., Benjamin F., "*Nanotechnology Enabled Sensors*", (Springer Book)

[6] Broers A. N., Hoole A. C. F., and Ryan J. M., "*Microelectronic Engineering*", 32 (1996), 131-142.

[7] Vander Pauw L. J., *Philips Res. Rep*, 20 (1958), 220.

[8] Montgomery H.C., *J.Appl.Phys*. 42 (1971), 2971.

CHAPTER 5

RESULTS AND DISCUSSION

This chapter discusses crystallographic, microstructural, compositional, magnetic, properties of Fe_xNi_{100-x}, Fe_xCo_{100-x} (x = 20, 40 and 80) and $Fe_{20}Ni_{80-x}Co_x$ (x = 20, 40 and 60).

5.1 Crystallography Study

Crystallographic studies were carried out after drying the samples and putting them into a sample holder via X-ray diffraction technique (XRD) at room temperature (Rigaku Ultimate VII) with CuKα (1.5418 Å) for all samples. Results are also discussed in this section.

5.1.1 X-ray diffraction Analysis of Fe_xNi_{100-x}

The crystallinity of the nanoalloy structures was determined using XRD from 2θ angle values of 20°–80°. Figure 5.1 shows the XRD patterns of the three compositions of Fe-Ni nanoalloys. It can be seen from the XRD patterns that the peaks at 44.42°, 51.8°, and 76.2° correspond to the crystal planes of (111), (200), and (220) of face-centered cubic (fcc) Fe_xNi_{100-x} alloy, respectively, which are in good agreement with already reported literature [1-4]. However, the XRD spectrum of $Fe_{80}Ni_{20}$ (x = 80 in Fig. 5.1) shows another additional peak at 35.7° (marked with an asterisk) indicating that the obtained alloy cannot be indexed to fcc FeNi alloy. This diffraction peak corresponds to a spinel oxide ($(FeNi)_3O_4$), which indicates that the formation of an oxide phase resulted in a high concentration of Fe precursor [1]. Generally, Fe-rich nanoparticles get more easily oxidized, and thus the formation of oxide phase could be obvious [1]. No diffraction patterns of pure metallic Fe or Ni are detected, indicating the absence of segregated metal NPs in the alloy

samples. The absence of pure Fe or Ni peak in XRD also indicates no phase separation in the bimetallic alloy [3]. Using the Scherrer equation from the full width at half maximum of the most intense XRD peak (111), the size of the Fe-Ni nanocrystallite was calculated to be 35 nm for all compositions. The size of the Fe-Ni nanocrystallite was found to be independent of composition, which indicates uniform fragmentation for a fixed sonication time and power.

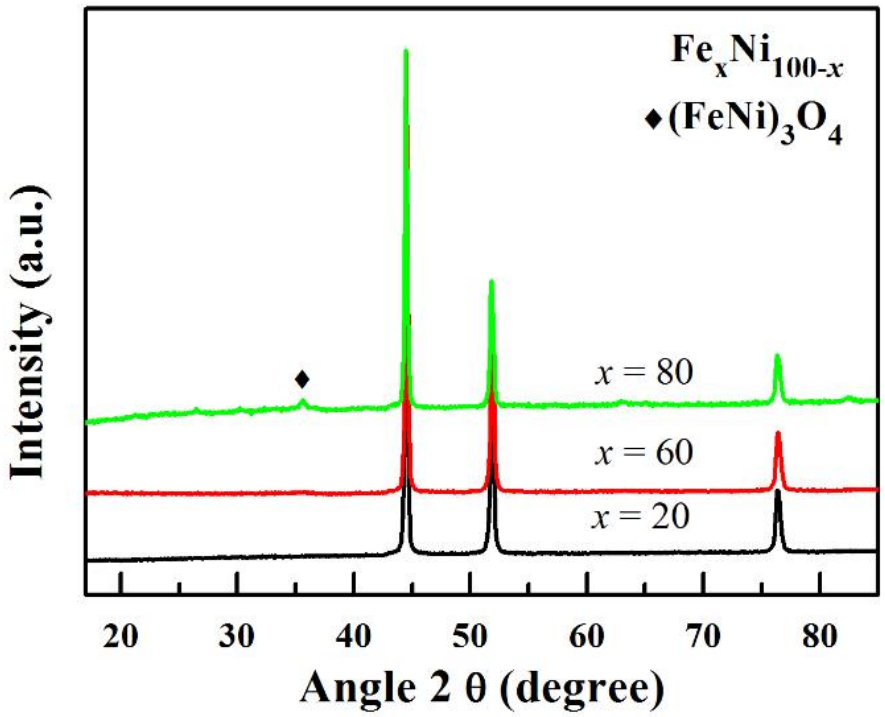

Figure 5.1 XRD pattern (from bottom to up) of $Fe_{20}Ni_{80}$, $Fe_{40}Ni_{60}$ and $Fe_{80}Ni_{20}$ binary nanoalloy.

5.1.2 X-ray diffraction Analysis of Fe_xCo_{100-x}

Fig. 5.2 shows the XRD patterns of the Fe_xCo_{100-x} (x = 20, 40 and 80) nanoalloys with varying compositions. It reveals from XRD patterns that, the peaks at 44.3°, 51.8°, and 76.2°correspond to the crystal planes of (111), (200), and (220), respectively which are in quite good agreement with the reported articles [5-7]. However, few representative Fe-Co peaks are missing which may be due to the exposure of the sample to air after synthesis may form oxide layer. In addition, the

diffraction peaks at 41.5°and 47.5° may represents FeO and Fe_3O_4, respectively [7]. Generally, Fe-rich NPs get easily oxidized, and thus the formation of oxide phase could be obvious [8]. No diffraction patterns of pure metallic Fe or Co are detected, which indicates the absence of any isolated metal in the alloy samples, and also confirms the absence of any phase separation in bimetallic alloy. Scherrer equation was used for the calculation of the size of the Fe-Co nanocrystallite, and found to be 19.3 nm for all composition. This demonstrates that the size of the Fe-Co nanocrystalline is independent of nanoalloy compositions, indicating uniform fragmentation due to fixed sonication time and power.

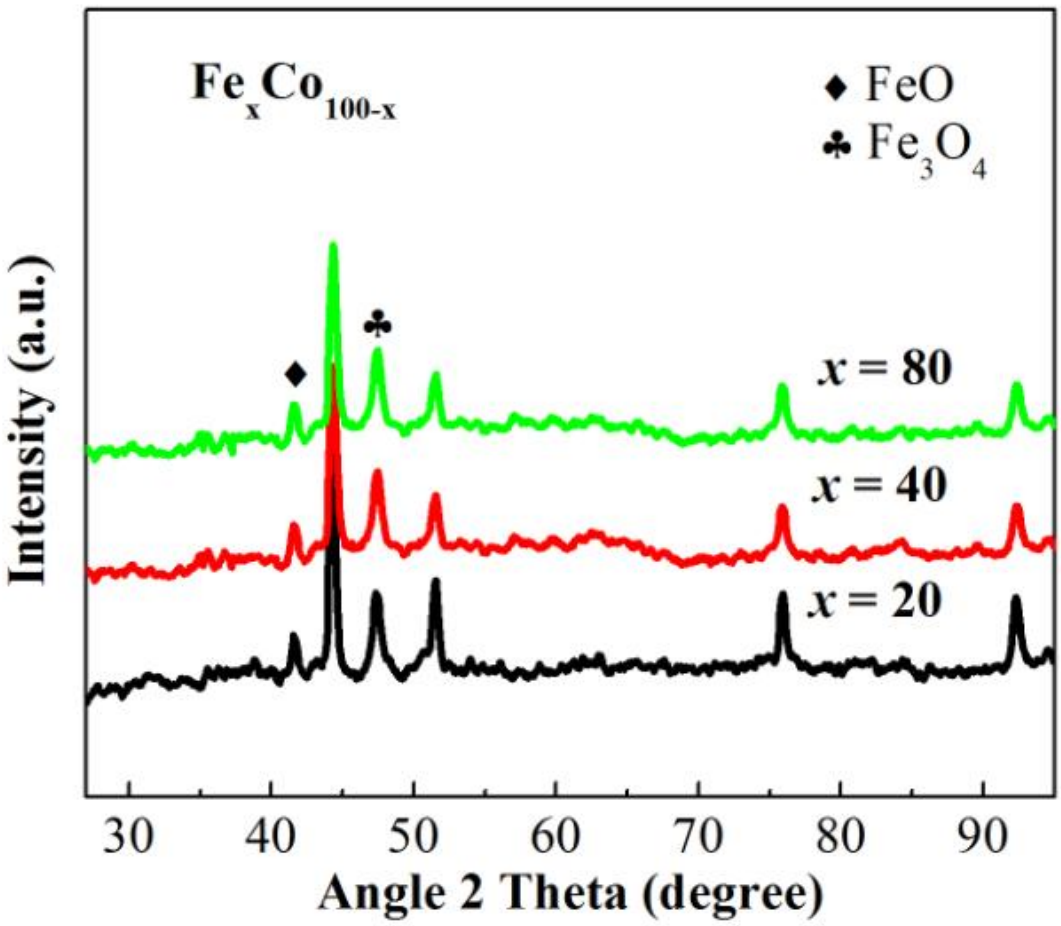

Figure 5.2 XRD pattern (from bottom to up) of $Fe_{20}Co_{80}$, $Fe_{40}Co_{60}$ and $Fe_{80}Co_{20}$ binary nanoalloy.

5.2 Microstructure Analysis

Microstructural studies for all samples were carried out by field emission scanning electron microscopy (FE-SEM) technique (S-4800, Hitachi) at an operating voltage of 3 kV. Samples diluted in 2-isopropanol were picked up by a dropper and placed into the sample holder. Results found are also discussed in this section for all Fe-Ni and Fe-Co samples.

5.2.1 FE-SEM Analysis of Fe_xNi_{100-x}

The SEM images of the synthesized Fe-Ni nanoalloy are presented in Fig. 5.3. From SEM images [see Fig. 5.3 (a)–(c)], it is clear that all Fe-Ni nanoalloy compositions under scrutiny exhibit a wide range of size distribution from 20 to 50 nm with rough surface and spherical shape morphology [see Fig. 5.3 (d)], and aggregated themselves to a cluster of particles.

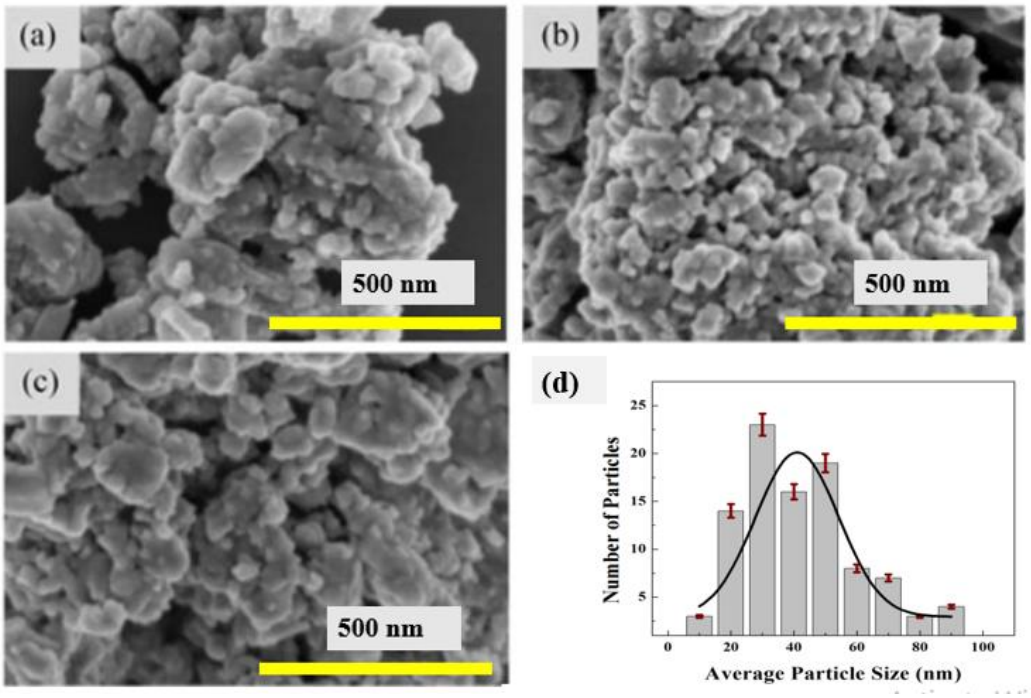

Figure 5.3. FE-SEM images of (a) $Fe_{20}Ni_{80}$, (b) $Fe_{40}Ni_{60}$, (c) $Fe_{80}Ni_{20}$, and (d) particle size distribution.

5.2.2 FE-SEM Analysis of Fe_xCo_{100-x}

Fig. 5.4 shows the FE-SEM images of the synthesized Fe-Co nanoalloy. All compositions of Fe-Co nanoalloy shows a wide range of size distribution from 5 to 100 nm with rough surface and spherical shape morphology [5.4 (a)–(c)]. In addition, the nanoparticles are aggregated themselves to a cluster of particles. A typical size distribution of the nanoparticles is shown in Figure 5.4 (d) which shows the average size of the particles were approximately 37 nm.

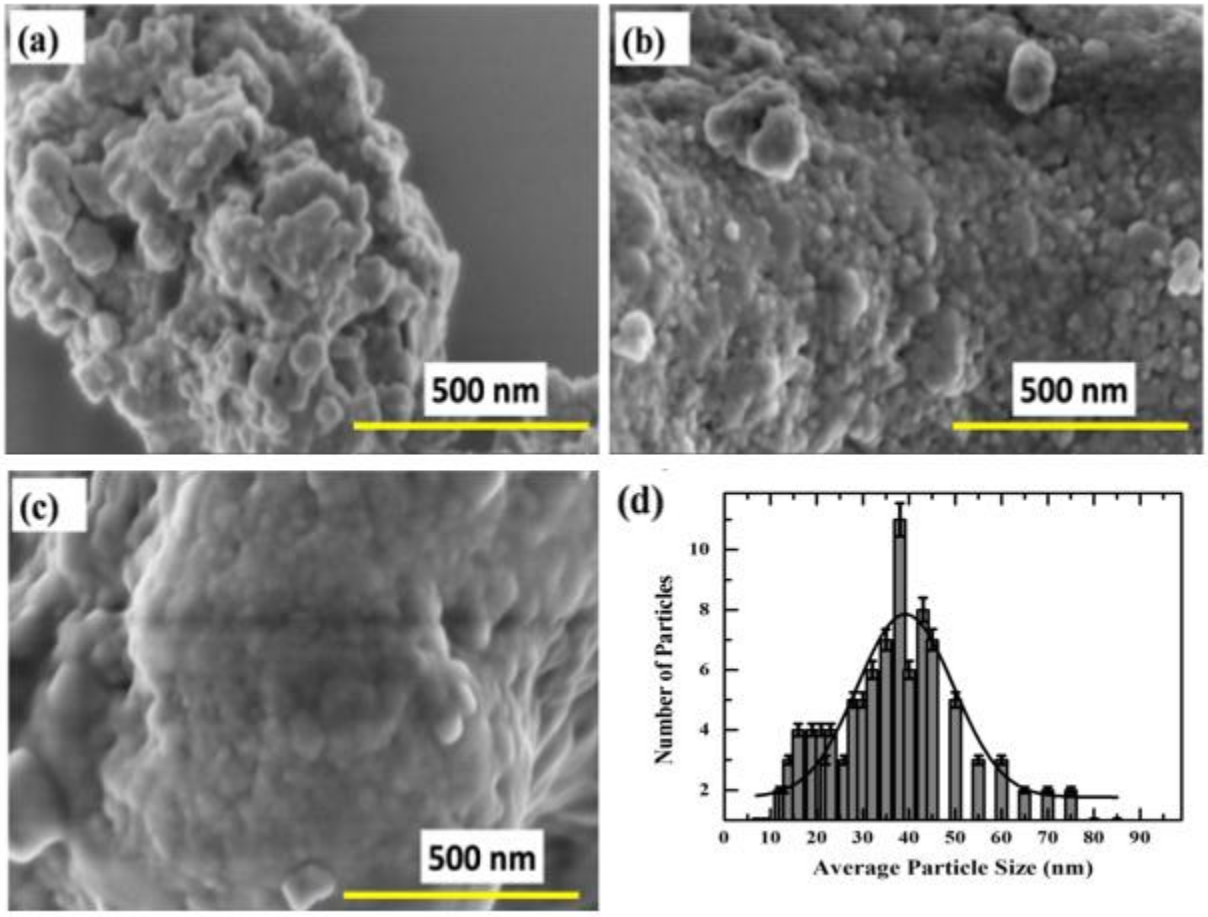

Figure 5.4: FE-SEM images of (a) $Fe_{20}Co_{80}$, (b) $Fe_{40}Co_{60}$, (c) $Fe_{80}Co_{20}$ and (d) particle size distribution.

5.3 Elemental Analysis

The elemental or compositional analysis for all samples were done by the Energy Dispersivepectroscopy (EDS) coupled with the FE-SEM. The operating voltage and probe current for the measurement of EDS system were 15 kV and 1.5 mA. Results are discussed in this section.

5.3.1 EDS Analysis of Fe_xNi_{100-x}

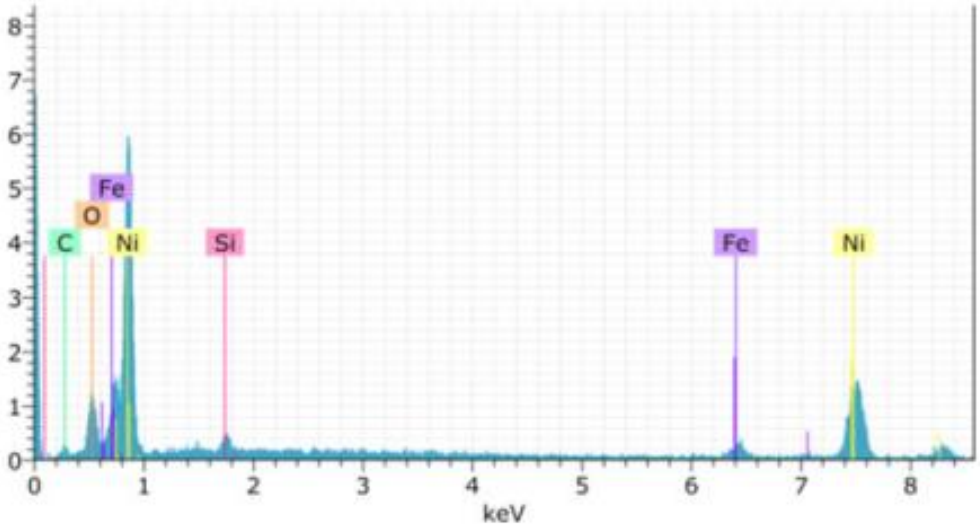

Figure 5.5: EDS spectra for $Fe_{20}Ni_{80}$.

The EDS analyses were conducted to obtain corresponding elemental composition of the nanoalloys. Fig. 5.5 shows a typical EDS spectrum for $Fe_{20}Ni_{80}$. Both Fe and Ni peaks are apparent in the spectrum. This result also confirmed the formation of Fe-Ni nanoalloy. As shown in Figure 5.5, the presence of silicon peak in the EDS spectrum may be due to the SiO_2 substrate used with the samples for EDS analysis. The occurrence of the O peak may be due to the oxidation of the nanoalloy. However, the XRD data do not show any oxidation peaks for the composition of $Fe_{20}Ni_{80}$ and $Fe_{40}Ni_{60}$ alloy, which indicates that there may be very thin or no crystalline oxidation layer on the surface or may be the SiO_2 substrate.

5.3.2 EDS Analysis of Fe_xCo_{100-x}

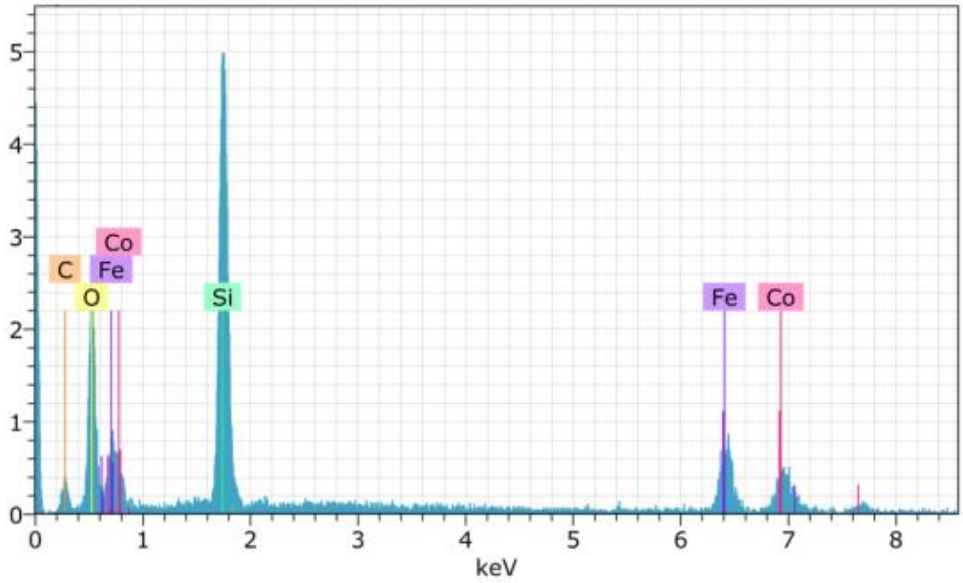

Figure 5.6: EDS spectra for $Fe_{80}Co_{20}$.

The EDS spectrum for $Fe_{80}Co_{20}$ is shown in Fig. 5.6 which indicates the presence of both Fe and Co elements in the vicinity of nanoalloy and confirmed the formation of Fe-Co bimetallic structure. There is a presence of a peak corresponds to silicon element in the EDS spectrum, which may be comes from the SiO_2 substrate, used for the sampling of NPs for EDS analysis. The presence of the O peak in the EDS spectrum is due to the thin oxidation layer of the nanoalloy. Fig. 5.7 shows the EDS mapping images of $Fe_{80}Co_{20}$ nanoalloy, which confirming the elements Fe and Co spatial distribution. Fig. 5.7 (a) shows the SEM image of $Fe_{80}Co_{20}$ nanoalloy, which is to be analyzed for EDS mapping. Fig. 5.7 (b)-(c) reveals the elemental maps of Fe and Co concentration, whereas Fig. 5.7 (d) shows the EDS mapping analysis of $Fe_{80}Co_{20}$nanoalloy. The elemental mapping result indicates the well distribution of all elements in the nanoalloy structures.

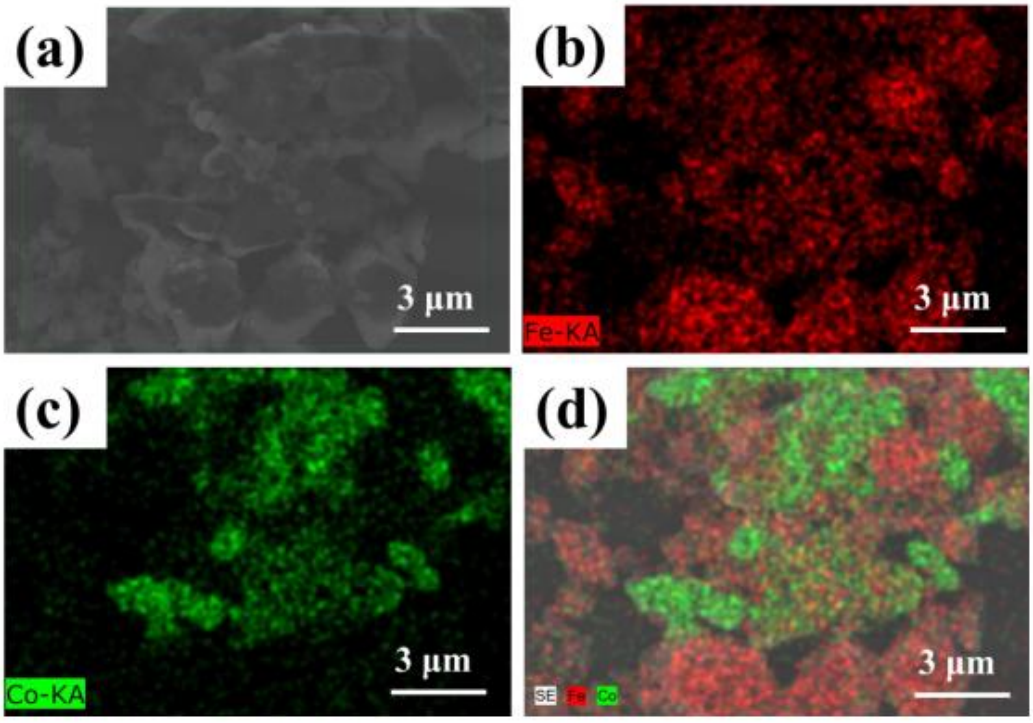

Figure 5.7: EDS mapping analysis of $Fe_{80}Co_{20}$; (a) SEM image of $Fe_{80}Co_{20}$ nanoalloy (b) map of Fe concentration (c) map of Co concentration (d) EDS mapping image of $Fe_{80}Co_{20}$ nanoalloy.

5.4 Magnetic Properties

The magnetic properties were measured for all samples using a VSM at room temperature (VSM, Lakeshore7400series) with a sensitivity of 10^{-6} emu at an applied field range of 10−10 kOe. The VSM measurement of the samples was done after complete drying of the samples. Found results are discussed in this section.

5.4.1 VSM Analysis of Fe_xNi_{100-x}

The magnetic properties of Fe-Ni nanoalloy were measured using VSM at room temperature to determine their saturation magnetization (Ms) and coercivity (Hc). Fig. 5.8 shows the M–H curves

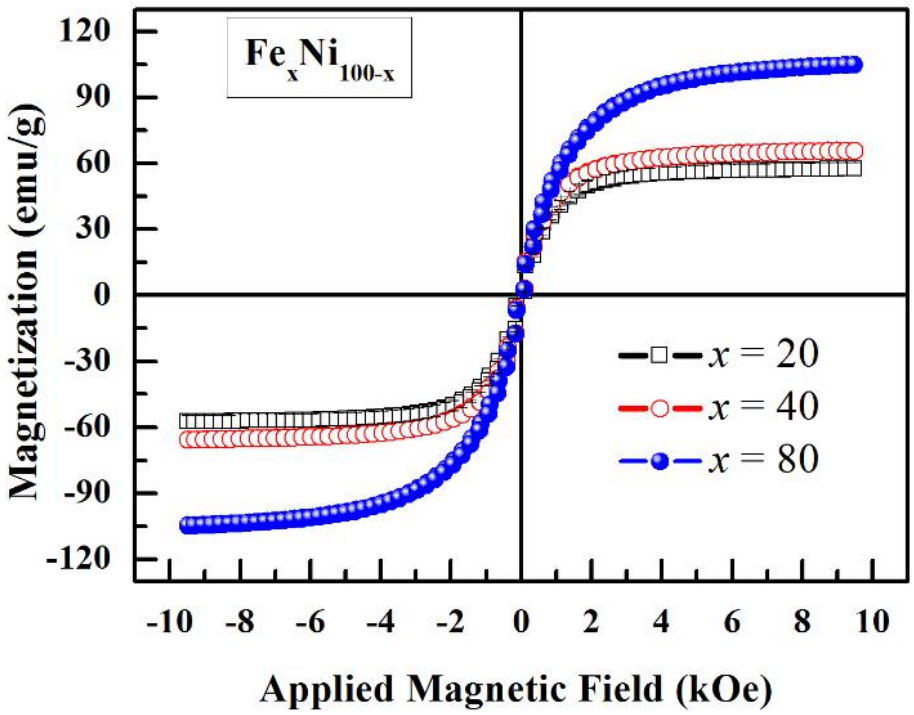

Figure 5.8: Magnetization versus magnetic field curves of Fe_xNi_{100-x} nanoalloy.

of Fe_xNi_{100-x} (x = 20, 60, and 80) measured in external magnetic fields ranging from −10 to 10 kOe. This is also observed that, the saturation magnetization increases with the increase of the Fe content in the Fe-Ni alloys (see Fig. 5.9). However, the coercivity decreases with the increase of the Fe content in the Fe-Ni alloy composition. The increased saturation magnetization is due to the incorporation of higher magnetic moment Fe atoms [1]. Moreover, there is a possibility of easy oxidation for more Fe content in the alloy, which was revealed in the XRD patterns. The maximum saturation magnetization and minimum coercivity were found to be 105 emu/g and 57 Oe for the composition $Fe_{80}Ni_{20}$, respectively, as shown in Fig. 5.9. Moreover the Mr/Ms values were found in the range of 0.07 to 0.08 indicating an appreciable fraction of superparamagnetic particles [9]. The decrease of the Fe content in an iron-based binary or ternary alloy decreases the coercivity [3], which is not indicated in Fig 5.8. Furthermore, in the framework of the Stoner–Wohlfarth

model [19], in the ideal case of well-separated fine particles, the Mr/Ms ratio is 0.5. Thus, the fact that the values of the Mr/Ms ratio of synthesized different Fe-Ni nanoalloy composition are found to be lower than 0.5 indicate relatively low interparticle distances between Fe-Ni nanoalloy in all compositions. In addition, it is interesting to note that the presently obtained results show a clear advance with those already reported in the literature, where they used different methods for synthesizing Fe-Ni, as shown in Table 5.1. Thus, such compositional dependent tunable magnetic properties of the Fe-Ni alloy can be used for various applications. The potential applications of the presently prepared nanoalloy are currently under investigation in various relative fields of nanomaterials and nanotechnology.

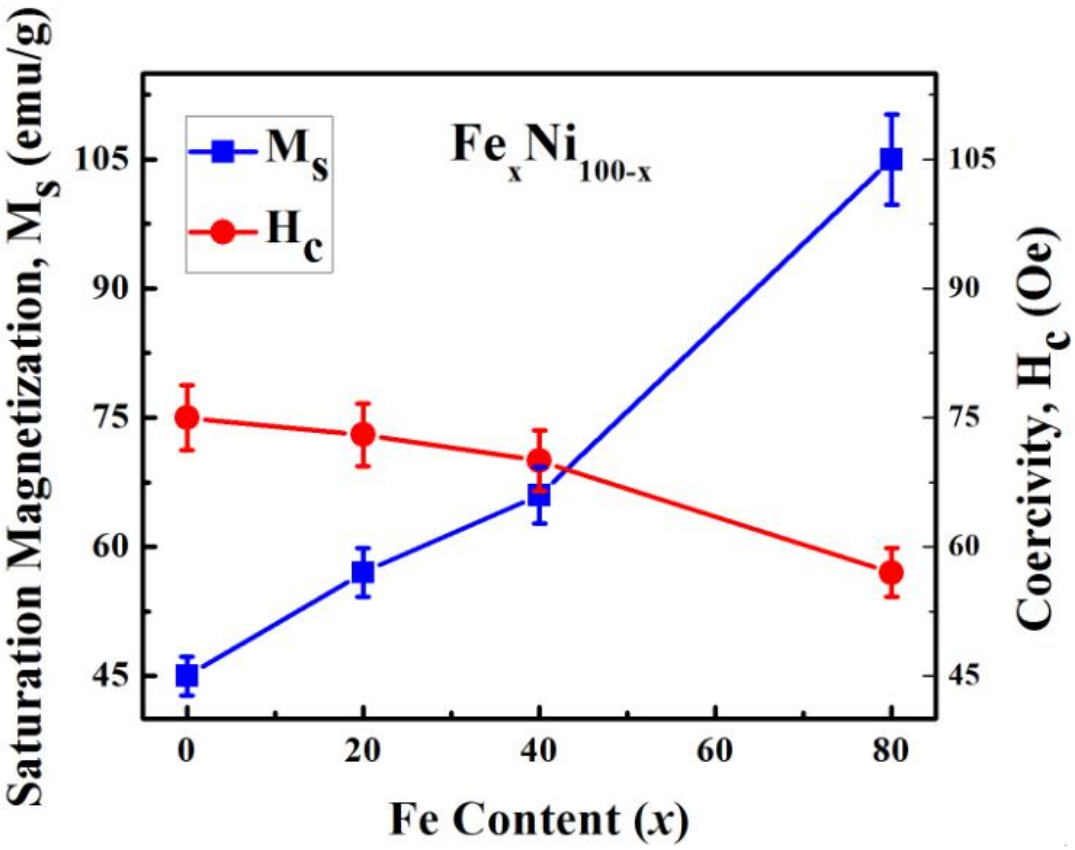

Figure 5.9: Variation of saturation magnetization and coercivity with Fe in Fe_xNi_{100-x} nanoalloy.

Table 5.1: Comparative study of reported magnetic properties of Fe-Ni nanoalloys prepared by using different synthesis methods.

Composition	M_s (emu/g)	H_c (Oe)	Synthesis Method	References
	69–90	150–100	Non-aqueous organometallic route	[1]
Fe-Ni	85, 40	100, 188	Coelectrodiposition	[2]
	97	250	Template based self-assembly	[4]
	57–105	73–57	Sonofragmentation	**Present work**

5.4.2 VSM Analysis of Fe_xCo_{100-x}

The VSM measurements at room temperature for Fe-Co nanoalloy were performed to determine the saturation magnetization (Ms) and coercivity (Hc). The measured M–H curves of Fe_xCo_{100-x} (x= 20, 60, and 80) in the external magnetic field ranging from -10 to 10 kOe are shown Fig. 5.10. From the M-H curve (Mr/Ms values shown in the Table 5.2), it can be understood that, the nanoalloy may shows superparamagnetic behavior [9]. By increasing the Fe content in Fe-Co alloy, the saturation magnetization increases. However, the coercivity decreases with the increase of the Fe content in the Fe-Co alloy composition. The increase in saturation magnetization and decrease in coercivity is may be due to the incorporation of higher magnetic moment Fe atoms in nanoalloy [19]. The maximum saturation magnetization and the minimum coercivity estimated from the M-H curve to be 153 emu/g and 80 Oe, respectively, for the composition of $Fe_{80}Co_{20}$, as shown in Fig. 5.11. Furthermore, according to the Stoner–Wohlfarth model [19], the Mr/Ms ratio is 0.5 for the ideal case of well-separated fine particles.

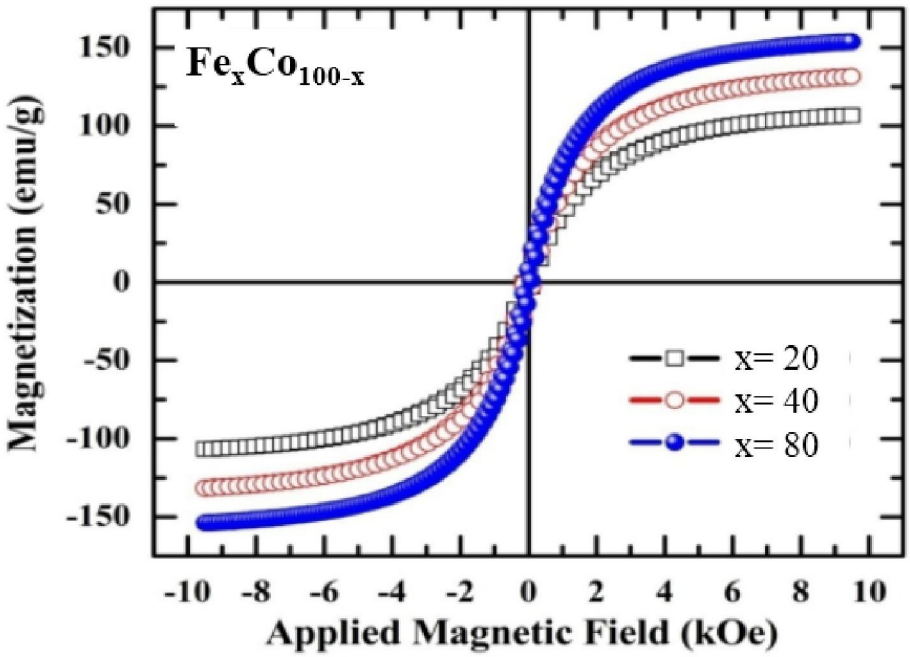

Figure 5.10: Magnetization versus magnetic field curves of Fe_xCo_{100-x} nanoalloy.

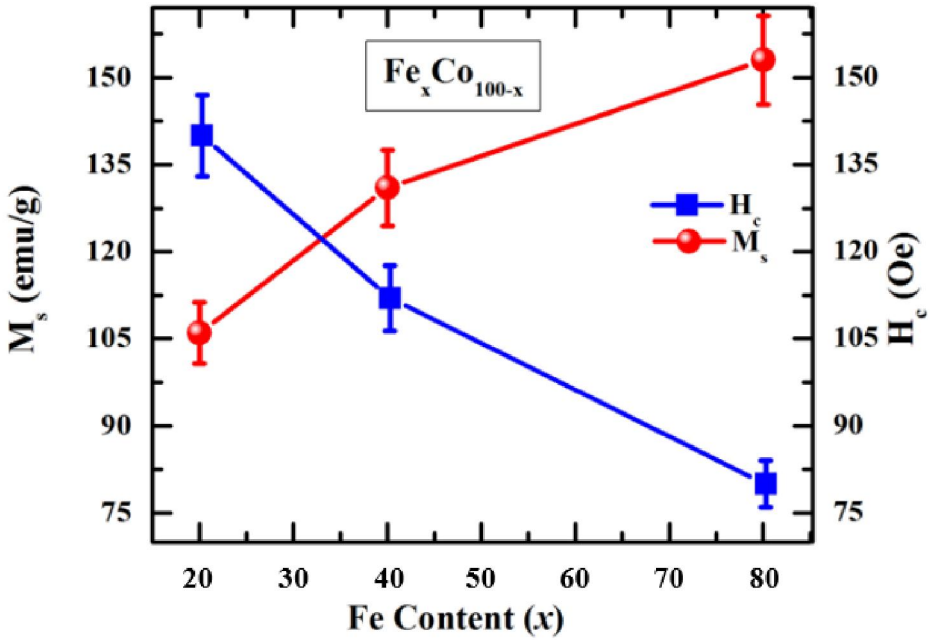

Figure 5.11: Variation of saturation magnetization and coercivity with Fe in Fe_xCo_{100-x} nanoalloy.

Table 5.2: Different parameters of magnetic properties for Fe_xCo_{100-x} nanoalloy.

Composition	Saturation Magnetization, M_s (emu/g)	Coercivity, H_c (Oe)	Reminance, M_r (emu/g)	M_r/M_s
$Fe_{20}Co_{80}$	107	128	11.14	0.10
$Fe_{40}Co_{60}$	131	113	9.50	0.07
$Fe_{80}Co_{20}$	153	72	8.45	0.06

Table 5.3: Comparative study of reported magnetic properties of Fe-Co nanoalloys at room temperature prepared by using different synthesis methods.

Composition	M_s (emu/g)	H_c (Oe)	Synthesis Method	References
Fe-Co	61	521	Co-precipitation	[6]
	200	212	Modified Polyol Process	[7]
	67	80	Surfactants-Assisted Ball Milling	[17]
	145	100	Thermal Decomposition	[23]
	107-153	128-72	Sonofragmentation	**Presented Work**

However, the values of the Mr/Ms ratio for different Fe-Co nanoalloy composition in the present are found to be lower than 0.5 which indicate that in all compositions the inter-particle distances between Fe-Co nanoalloy relatively low, as shown in Table 5.2. The present obtained results show a clear advance than those already reported in the literature, as shown in Table 5.3. Thus, such compositional dependent tunable magnetic properties of the Fe-Co alloy can be used for various practical applications.

5.5 $Fe_{20}Ni_{80-x}Co_x$ Nanoalloy

Besides these Fe-Ni and Fe-Co discussed above, Fe-Ni-Co samples were also synthesized using the same sonofragmentation technique. Crystallographic, morphological, elemental and magnetic studies were completed using the same XRD, SEM, EDS and VSM respectively.

5.5.1 X-ray Diffraction Analysis of $Fe_{20}Ni_{80-x}Co_x$

The crystallographic structure of the synthesized nanoalloy was determined from powder XRD diffraction. Figure 5.12 shows the XRD patterns of $Fe_{20}Ni_{80-x}Co_x$, x = 20, 40 and 60. The intensity peaks were observed at 44.52°, 51.8°, and 76.2° in the XRD patterns which correspond to the crystal planes of (111), (200), and (220) of face-centered cubic (fcc) $Fe_{20}Ni_{80-x}Co_x$ alloy respectively. This result is consistent with the ones reported in previous investigations where structural characterizations of Fe-Ni-Co ternary alloys synthesized by different methods i.e. hydrogen plasma metal reaction, mechanical alloying were performed [10-14]. However, the XRD spectrum of Co rich $Fe_{20}Ni_{20}Co_{60}$ shows two additional low intensity peaks (< 5%) at 41.7° and 47.5° (marked with star) indicating that the obtained alloy cannot be indexed to fcc Fe-Ni-Co alloy. These diffraction peaks correspond to hexagonal close-packed (hcp) Co [15-17], as Co is much brittle and thus more prone to fragmentation and dispersion than Ni during the alloying process [15]. No diffraction patterns of pure metallic Fe, Co, Ni are detected in other (x= 20 and 40) samples, indicating the absence of segregated metal nanoparticles in the alloy samples. In addition the absence of oxide peaks denoted the purity of the synthesized samples. Using the Scherrer equation from the full width at half maximum (FWHM) of the most intense XRD peak (111), the size of the $Fe_{20}Ni_{80-x}Co_x$ nanocrystallite was calculated to be 34 nm, 31nm, 24 nm for x= 20, 40 and 60 respectively. The lattice constants for Fe–Ni–Co ternary alloys are found to be in the range

3.5202–3.5247 Å. It may be interpreted that in synthesized ternary alloy, Fe atoms are embedded in the fcc Co–Ni alloy matrix [11]. The lattice constants of the nanoalloys with Co and Ni content variation is shown in Table 5.4.

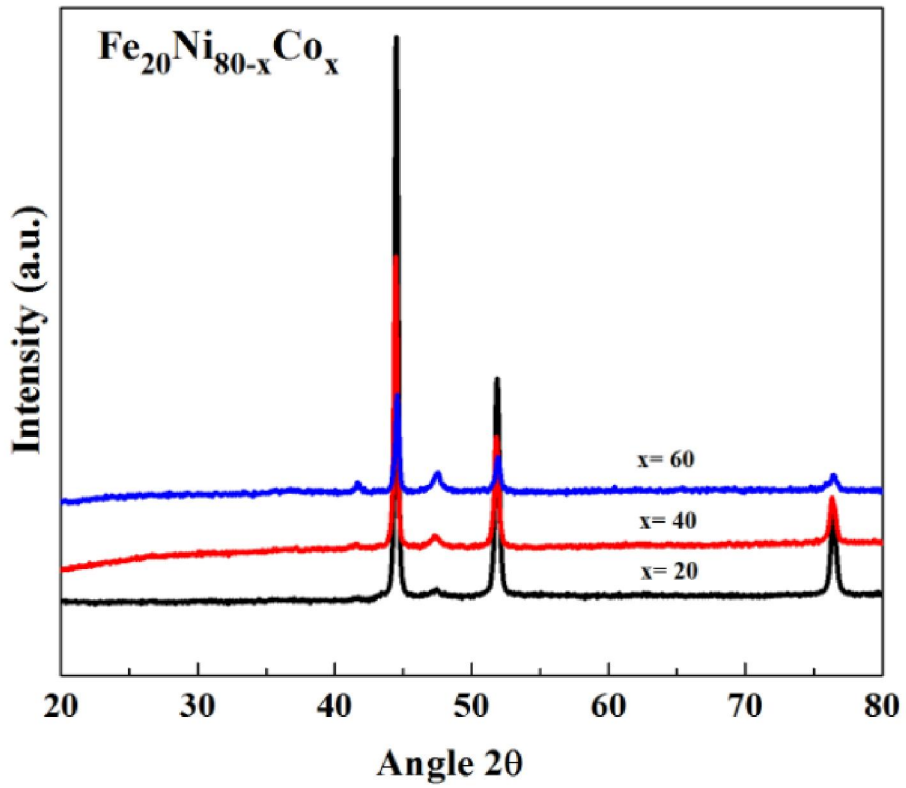

Figure 5.12: XRD pattern of $Fe_{20}Ni_{80-x}Co_x$ (from bottom x= 20, 40, 60) ternary nanoalloy.

Table 5.4 Composition, FWHM, crystallite size and lattice constant of $Fe_{20}Ni_{80-x}Co_x$, x = 20, 40 and 60.

Compositions	FWHM (degree)	Crystalline Size (nm)	Lattice Constant, a (Å)
$Fe_{20}Ni_{60}Co_{20}$	0.2652	34	3.5202
$Fe_{20}Ni_{40}Co_{40}$	0.2886	31	3.5202
$Fe_{20}Ni_{20}Co_{60}$	0.3737	24	3.5247

5.5.2 FE-SEM Analysis of $Fe_{20}Ni_{80-x}Co_x$

The FE-SEM images of the synthesized Fe-Ni-Co nanoalloy are presented in Figure 5.13. The SEM images [see Figure 5.13 (a)–(c)], indicate that all Fe-Ni-Co nanoalloy compositions under scrutiny exhibit a wide range of size distribution with spherical shape morphology, and aggregated themselves to a cluster of particles. The agglomeration of particles is due to high cold welding rate of the Fe-Ni-Co nanoparticles [18]. Figure 5.13 (d) shows the particle size distribution of Figure 5.13 (a) calculated with Image J. This Figure 5.13 (d) also indicates that most of the particles are between 30 nm to 50 nm.

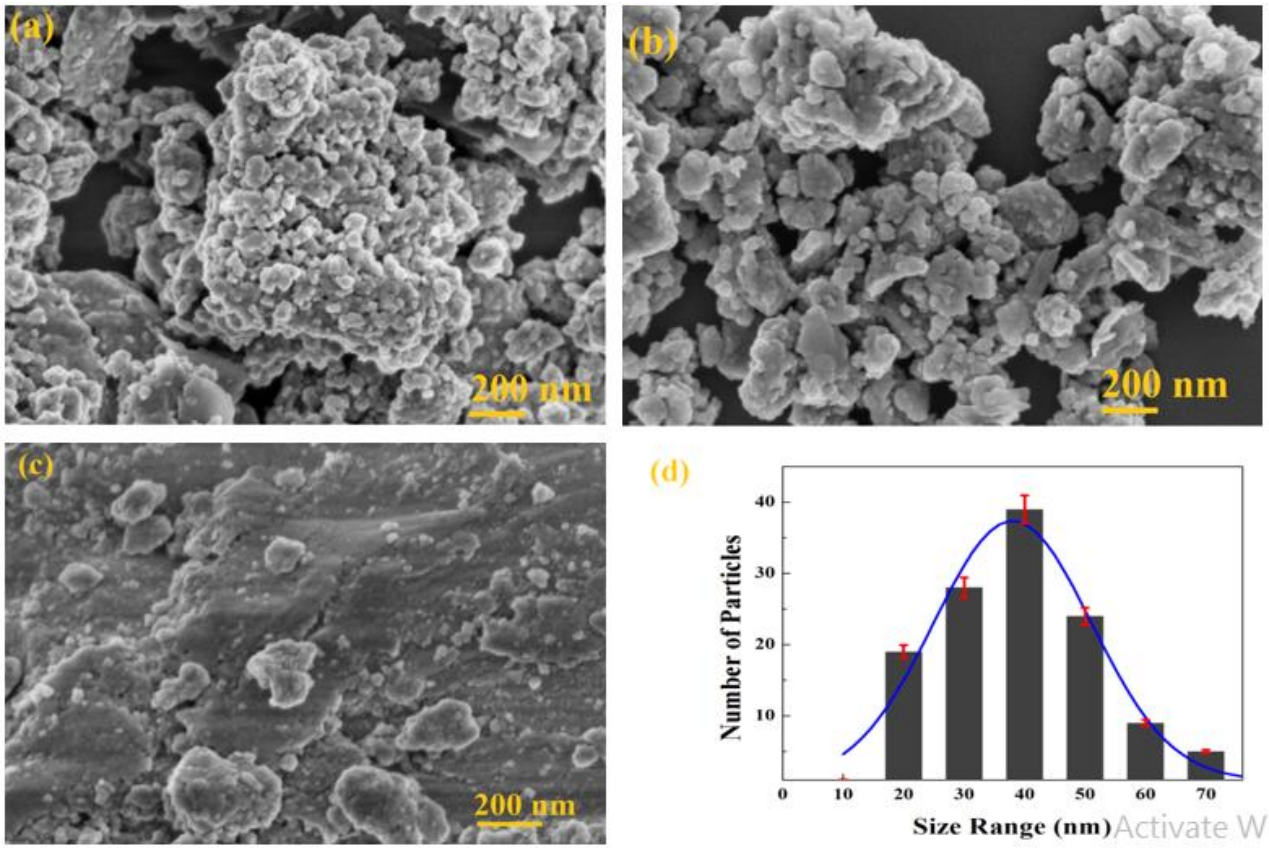

Figure 5.13: FE-SEM images of $Fe_{20}Ni_{80-x}Co_x$, (a) x=20, (b) x=40, (c) x=60, (d) Particle size distribution in Figure (a).

5.5.3 EDS Analysis of $Fe_{20}Ni_{80-x}Co_x$

The EDS analyses were conducted to obtain corresponding elemental composition of the nanoalloys. Fig. 5.14 shows a typical EDS spectrum for $Fe_{20}Co_{20}Ni_{60}$. All Fe, Co and Ni peaks are apparent in the spectrum. This result also confirmed the formation of Fe-Ni-Co nanoalloy. The occurrence of the O peak may be due to the oxidation of the nanoalloy. However, the XRD data do not show any oxidation peaks for the composition of $Fe_{20}Co_{20}Ni_{60}$ alloy, which indicates that there may be very thin or no crystalline oxidation layer on the surface. The EDS mapping analysis of the same sample is also shown in Fig. 5.15. It was observed that Fe, Co and Ni alloy particles had almost homogenous compositional distribution throughout the mixture.

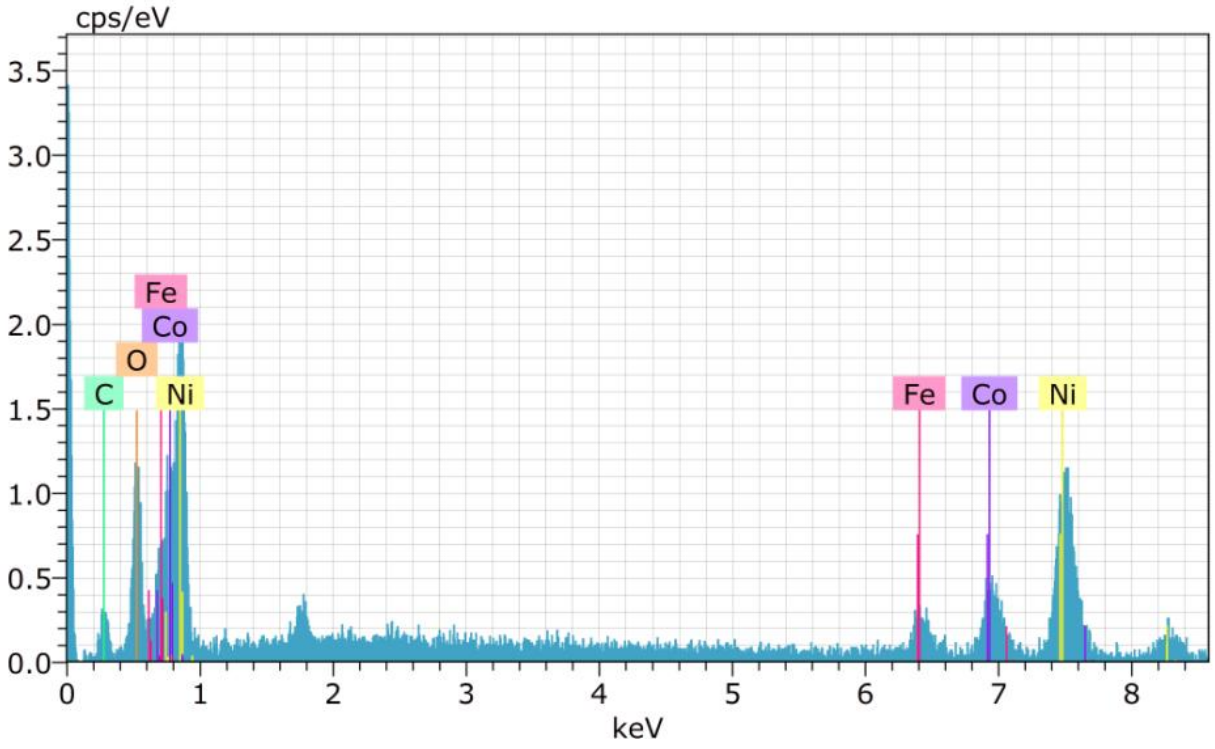

Figure 5.14: EDS spectra for $Fe_{20}Co_{20}Ni_{60}$.

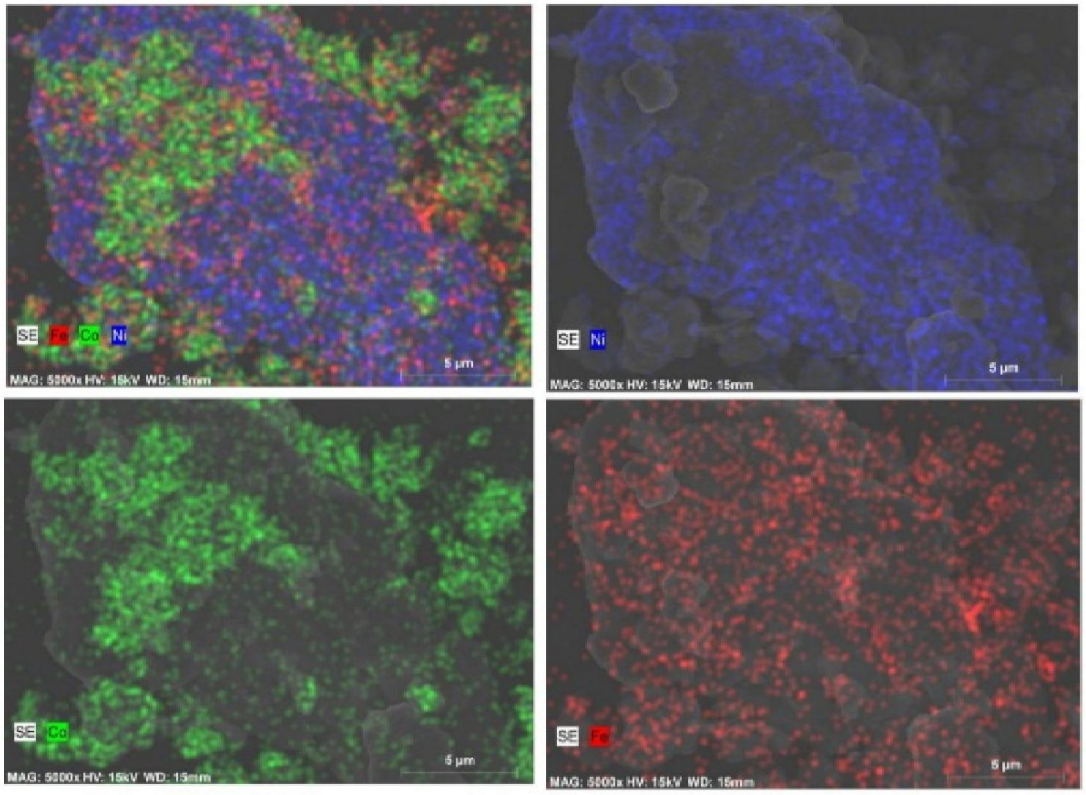

Figure 5.15: The EDS map of the $Fe_{20}Co_{20}Ni_{60}$ particles.

5.5.4 VSM Analysis of $Fe_{20}Ni_{80-x}Co_x$

The magnetic properties of the synthesized Fe-Ni-Co ternary nanoalloy were measured using VSM to determine their coercivity and saturation magnetization. Figure 5.16 shows the M–H hysteresis loops of $Fe_{20}Ni_{80-x}Co_x$ (x = 20, 40 and 60) carried out at room temperature with an applied magnetic field of up to ±10 kOe. The coercive field (H_c) is quantified by $H_c = (H_{c1}-H_{c2})/2$ where Hc_1 and Hc_2 are the left and right coercive fields, respectively [24, 25]. The values of coercivity (Hc), saturation magnetization (Ms) and reduced remanence (Mr/Ms) extracted from figure 5.16 are shown in Table 5.5.

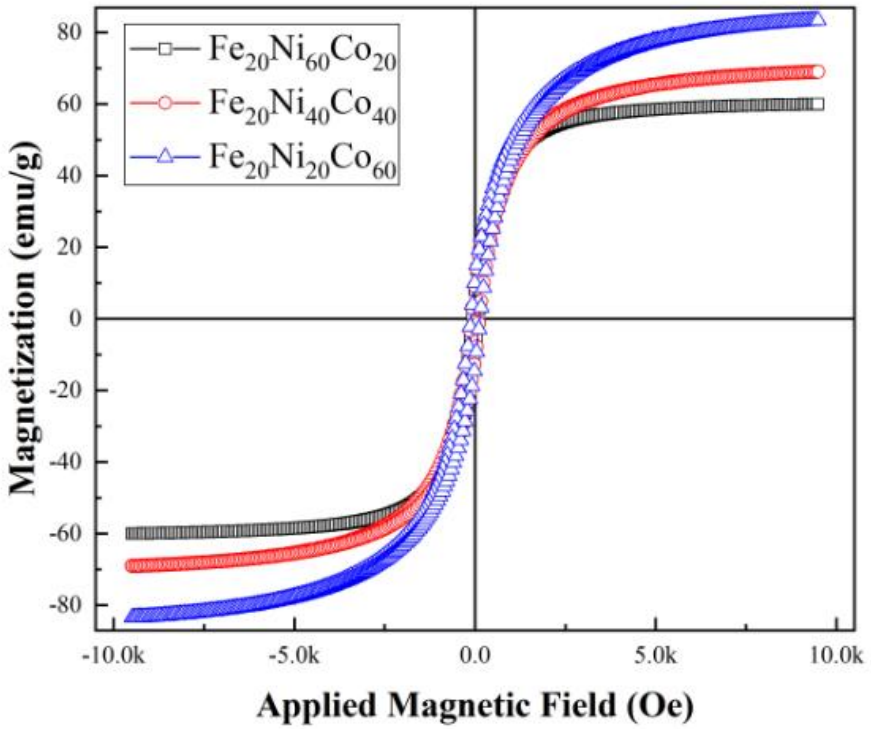

Figure 5.16: Magnetization versus magnetic field curves of $Fe_{20}Ni_{80-x}Co_x$ (x = 20, 40 and 60) nanoalloy.

The coercive field changed in the range of 79–115 Oe and saturation magnetizations of samples varied in the range of 60–83 emu/g. Both the saturation magnetization and coercivity increase with the increase of the Co content, reversely decrease with Ni in the Fe-Ni-Co alloys [shown in Table 5.5], which is also in agreement with Ref. [20]. The increased saturation magnetization may be due to the incorporation of the higher magnetic moment of Co atoms as compared to Ni (atomic magnetic moments of Co and Ni are 2.48 μB and 1.26 μB respectively, μB= Bohr Magneton) [19, 21]. The values of reduced remanence (also called squareness ratio) indicate the superparamagnetic behavior of synthesized Fe-Ni-Co ternary alloys [22]. Notably, in the ideal case of well-separated fine particles, the Mr/Ms ratio is 0.5 [19]. Thus, the fact that the values of the Mr/Ms ratio of synthesized different Fe-Ni-Co nanoalloy composition are found to be lower than

0.5 indicates relatively low interparticle distances between Fe-Ni-Co nanoalloy in all compositions. The reduced remanence of synthesized Fe-Ni-Co alloys decreases almost linearly with increasing Co content [shown in Table 5.5] implying that the addition of Co has a direct relation to the softness of the synthesized particles.

Table 5.5: Composition, coercivity, saturation magnetization and reduced remanence of $Fe_{20}Ni_{80-x}Co_x$, x = 20, 40 and 60.

Compositions	**H_c (Oe)**	**M_s (emu/g)**	**M_r/M_s**
$Fe_{20}Ni_{60}Co_{20}$	79.5	60	0.14
$Fe_{20}Ni_{40}Co_{40}$	95.9	69	0.135
$Fe_{20}Ni_{20}Co_{60}$	114.7	83	0.13

A comparative study of previously reported magnetic properties of Fe-Ni-Co nanoalloys prepared via different synthesis methods is presented in Table 5.6 which shows that our present work has made a clear improvement in different properties of the synthesized materials. For instance, in Ref [11] the authors synthesized $Fe_{20}Ni_{60}Co_{20}$ nanoparticles with a composition similar to the current study by sodium borohydride reduction method using many toxic and costly precursors and reported the coercivity and saturation magnetization to be 148 Oe and 54.3 emu/g respectively. On the contrary, in the present investigation, coercivity and saturation magnetization of the same nanocomposite synthesized by sonofragmentation method are reported to be 79 Oe and 60 emu/g. Table 5.6 also shows variations in the crystal size and magnetic properties of the nanoalloys with changing compositional contents which have been discussed earlier. Such composition dependent tunable magnetic properties of the Fe-Ni-Co alloy can be used extensively for various applications.

Also, the potential applications of the presently prepared nanoalloys are under investigation in different fields of nanomaterials and nanotechnology in recent times.

Table 5.6: Comparative study of reported magnetic properties of Fe-Ni-Co nanoalloys prepared via different synthesis methods.

Compositions	**Crystalline Size (nm)**	**H_c (Oe)**	**M_s (emu/g)**	**Synthesis Route**	**Reference**
$Fe_{20}Ni_{60}Co_{20}$	27	148	54	Sodium borohydride reduction (SBR)	[11]
$Fe_{33}Ni_{33}Co_{34}$	52	29	122	Hydrogen reduction assisted ultrasonic spray pyrolysis (HR-USP)	[13]
$FeNi_{16.5}Co_{16.5}$	-	116	43	Mechanical alloying and hydrogen reduction	[18]
$Fe_{50}Ni_{40}Co_{10}$	36	327	126	Chemical reduction	[20]
$Fe_{20}Ni_{80}$	35	73	57	Sonofragmentation	**Present work**
$Fe_{20}Ni_{60}Co_{20}$	34	79	60	Sonofragmentation	**Present work**
$Fe_{20}Ni_{40}Co_{40}$	31	96	69	Sonofragmentation	**Present work**
$Fe_{20}Ni_{20}Co_{60}$	24	115	83	Sonofragmentation	**Present work**

References

[1] Chen Y, Luo X, Yue G H, X Luo, Peng D L, "Synthesis of iron–nickel nanoparticles via a nonaqueous organometallic route*," Mater. Chem. Phys.*, 113(2009), 412–416.

[2] Moghimi N, Rahsepar F R, Srivastava S, Heinig N, Leung K T, "Shape-dependent magnetism of bimetallic FeNi nanosystems," *J. Mater. Chem. C*, 2 (2014), 6370–6375.

[3] Sharma H, Jain S, Raj P M, Murali K P Tummala R, "Magnetic and dielectric property studies in Fe- and NiFe- based polymer nanocomposites," *J. Electron. Mater*, (2015).

[4] Zhou J, Jiao T, Guo W, Wang B, Guo H, Cui L, Zhang Q, Chen Y Peng Q, "Preparation of iron-nickel alloy nanostructures via two cationic pyridinium derivatives as soft templates," *Nanomater. Nanotechnol*., 5 (2015), 25.

[5] Kandapallil B., Colborn R. E., Bonitatibus P. J., Johnson F, *J. Magn. Magn. Mater*., 378 (2015), 535–538.

[6] Hesani M., A. Yazdani, B. R. Abedi, M. Ghazanfari, *Solid State Comm*., 150 (2010), 594-597.

[7] Zachary J. H., Kyler J. C., Everett E. C., *J. Appl. Phys*., 109 (2011), 07B514.

[8] Zehani K., Bez R., Boutahar A., Hlil E. K., Lassri H., Moscovici, Mliki, Bessais, *J. Alloys and Comp*., 591 (2014), 58–64.

[9] Rashad M.M., Magnetic properties of nanocrystalline magnesium ferrite by co-precipitation assisted with ultrasound irradiation, *J. Mater Sci.*, 42(2007), 5248.

[10] Pikula T., Oleszak D., Pekata M., Jartych E., Structure and some magnetic properties of mechanically synthesized and thermally treated Co–Fe–Ni alloys, *J. Magn. Magn. Mater*. 320 (2008), 413–420.

[11] Dalavi S. B., Theerthagiri J., Raja M. M., Panda R.N., Synthesis, characterization and magnetic properties of nanocrystalline $Fe_xNi_{80-x}Co_{20}$ ternary alloys, *J. Magn. Magn. Mate*r. 344 (2013) 30–34.

[12] Gómez-Esparza C. D., Baldenebro-López F.J., Santillán-Rodríguez C. R., I. Estrada-Guel I., Matutes-Aquino, Herrera-Ramírez, Martínez-Sánchez, Microstructural and magnetic behavior of an equiatomic NiCoAlFe alloy prepared by mechanical alloying, *J. Alloys Comp*. (2014), http://dx.doi.org/10.1016/j.jallcom.2014.01.233.

[13] Toparlia C., Ebin B., Gürmen S., Synthesis, structural and magnetic characterization of soft magnetic nanocrystalline ternary FeNiCo particles, *J. Magn. Magn. Mater*. 423 (2017) 133–139.

[14] Li X., Takahashi S., Synthesis and magnetic properties of Fe-Ni-Co nanoparticles by hydrogen plasma metal reaction, *J. Magn. Magn. Mater.,* 214 (2000) 195-203.

[15] Prasad N. K., Kumar V., Structure–magnetic properties correlation in mechanically alloyed nanocrystalline Fe–Co–Ni–$(Mg–Si)_x$ alloy powders, *J. Mater. Sci.: Mater Electron* (2016).

[16] Baghbaderani H. A., Sharafi S., Chermahini M. D., Investigation of nanostructure formation mechanism and magnetic properties in $Fe_{45}Co_{45}Ni_{10}$ system synthesized by mechanical alloying, *Powder Technology,* 230 (2012).

[17] Poudyal N., Rong C., and Liu J. P., Morphological and magnetic characterization of Fe, Co, and FeCo nanoplates and nanoparticles prepared by surfactants assisted ball milling, *J. Appl. Phy.* 109 (2010), 07B526.

[18] Azizi A., Yoozbashizadeh H, Sadrnezhaad S.K., Effect of hydrogen reduction on microstructure and magnetic properties of mechanochemically synthesized $Fe_{16.5}Ni_{16.5}Co$ nano-powder, *J. Magn. Magn. Mater*., 321 (2009).

[19] B. Sinha, R. Tanveer, T. S. Ramulu, Z. M. Ahsan, R. S. Mahabubur, and M. A. Basith, *IEEE Magnetics Letters*, 8 (2017), 4108404.

[20] Chokprasombat K., Pinitsoontorn S., Maensiri S., Effects of Ni content on nanocrystalline Fe-Ni-Coternary alloys synthesized by a chemical reduction method, *J. of Magn. Magn. Mater*., vol. 405 (2016).

[21] Ota N., Magnetic moment and band structure analysis of Fe, Co, Ni-modified Graphene-nano-ribbon, Cornell Univ. Library, *Mesoscale and Nanoscale Physics* (2104), https://arxiv.org/ftp/arxiv/papers/1401/1401.4504.pdf.

[22] Goya G.F., Rechenberg H.R., Superparamagnetic transition and local disorder in $CuFe_2O_4$ nanoparticles, *Nanostructured Materials*, vol. 10 (1998), 6, 1001-1011.

[23] Tzitzios V., Basina G., Niarchos D., Wanfeng L., G. Hadjipanayis, *J. Appl. Phys.,*109 (2011), 07A313.

[24] Basith M. A., Khan F. A., Ahmmad B., Kubota S., Hirose F., Ngo D.-T., Mølhave K., Tunable exchange bias effect in magnetic $Bi_{0.9}Gd_{0.1}Fe_{0.9}Ti_{0.1}O_3$ nanoparticles at temperatures up to 250 K, *J. Appl. Phy*., 118(2015), 023901.

[25] Ahammad B., Islam M. Z., Billah A., Basith M. A., Anomalous coercivity enhancement with temperature and tunable exchange bias in Gd and Ti co-doped $BiFeO_3$ multiferroics, *J. Phy. D: Appl. Phy*., 49 (2016), 095001.

CHAPTER 6

CONCLUSION

6.1 Overview

Finally, a facile and cost-effective sonofragmentation approach for the synthesis of FeNi and FeCo nanoalloys with various compositions of Fe, Ni and Co have been demonstrated successfully. We used only the ultrasonic energy for the fragmentation of bigger particles, and no additional reducing or reacting agents are used for the synthesis of alloy nanoparticles. The XRD results exhibited negligible impurity phases for Fe-Ni and Fe-Ni-Co sample though in Fe-Co iron got oxidized a little more than other samples. This limitation can be easily avoided via inclusion of better sintering in synthesis method. SEM results showed that the nanoalloy particles are aggregated in nature with wide size distribution. Although, further work is required to control particle size and shape since it is an initiation of the use of sonofragmentation technique for the synthesis of nanoalloy which is cost effective, toxicants free, and environmental friendly. Significant modifications in the magnetic properties are obtained by changing the composition of both Fe-Ni and Fe-Co nanoalloys. In particular, the saturation magnetization increases with the increased Fe content in both Fe-Ni and Fe-Co alloy. Furthermore, a half-time reduced coercivity of the reported value is found for $Fe_{80}Ni_{20}$ composition than other composition of the Fe-Ni alloy. The crystal size has been found to be decreasing with increasing Co content along with increasing softness in the magnetic nature in cases of Fe-Ni-Co ternary nanoalloys. The synthesized high magnetization Fe-Ni and Fe-Co nanoalloy can be used for various potential applications, and also this simple technique can be extended to synthesize other nanoalloys.

6.2 Limitations

With several advantages like environment friendliness or inexpensive and short synthesis route, sonofragmentation still have some limitations. In this method sizes and shapes of the synthesized particles could not be controlled. Moreover the particles were found agglomerated from the SEM image and monodispersed particles were not noticed. However furthers modifications are needed to this method like changing the grinding or sonication time or inclusion of better calcination or sintering technique.

6.3 Future Work

- More works can be done to control the shape and size of the synthesized particles, particularly by extending and reducing the sonication time.
- Complex nanostructures of different organic or inorganic compound can be attempted to synthesize applying this sonofragmentation technique.
- In some cases particles especially Fe got oxidized by surrounding. Therefore, more works are needed to be done to control this oxidation of the synthesized particles like inclusion of higher vacuum or better sintering.
- Further works can be conducted to achieve mono-dispersed particles.
- Changes in crystal size, coercivity and saturation magnetization could be further investigated with more different compositions of Fe, Ni and Co.

PUBLICATION LIST

Papers in peer-review journals

Rubayet Tanveer, Brajalal Sinha, Sri Ramulu Torati, Mohammed Abdul Basith. Magnetization Controlled Synthesis of FeCo Nanoalloys Using Facile Sonofragmentation Approach (Under Review), Indian Journal of Pure and Applied Physics.

Brajalal Sinha, **Rubayet Tanveer**, Sri Ramulu Torati, M Ziaul Ahsan, M Rahman Shah and Md, Mohammed Abdul Basith. A Simplistic Sonofragmentation Approach for Synthesis of NiFe Nanoalloy with Tunable Magnetization. IEEE Magnetics Letters, Volume8 (2017), LM AG-17-06-SM-0094, DOI: 10.1109/LMAG.2017.2740385.

Selected presentations in conferences

Rubayet Tanveer, Brajalal Sinha, Mohammed Abdul Basith and Sriramulu Torati. Magnetic Properties of Simple top down Sonofragmented Co-Fe Nanoparticles. International Conference on Physics-2018, Bangladesh Physical Society, 08-10 March, 2018.

Rubayet Tanveer, Brajalal Sinha, M Ziaul Ahsan, Mahabubar Rahman Shah, Rumana Maleque, Mohammed Abdul Basith. Synthesis of Magnetic Binary Alloy Nanoparticles by Sonofragmentation Process. International Conferenceon Nanotechnology and Condensed Matter Physics (ICNCMP), BUET, Dhaka, 11-12 Jan 2018.

Rubayet Tanveer, Brajalal Sinha, M Ziaul Ahsan, Mahabubar Rahman Shah, Mohammed Abdul Basith and Sriramulu Torati. A Facile Route for Synthesis Ni-Fe Nanoparticles by Sonofragmentation Process. International Conference on Mechanical Engineering & Applied Science (ICMEAS), Dhaka, 2017 Feb 22-23; 222.

APPENDIX

Nanomagnetics

Simple Sonofragmentation Approach for Synthesis of Ni-Fe Nanoalloy With Tunable Magnetization

Brajalal Sinha[1], Rubayet Tanveer[1], Sri Ramulu Torati[2], M. Ziaul Ahsan[1], M Rahman Shah[1], and M. A. Basith[3]

[1] *Military Institute of Science and Technology, Dhaka 1216, Bangladesh*
[2] *School of Chemical and Biotechnology, SASTRA University, Thanjavur 613401, India*
[3] *Department of Physics, Bangladesh University of Engineering and Technology, Dhaka 1000, Bangladesh*

Received 5 Jun 2017, revised 26 Jul 2017, accepted 31 Jul 2017, published 17 Aug 2017, current version 12 Sep 2017.

Abstract—$Ni_{1-x}Fe_x$ ($x = 0.20$, 0.40, and 0.80) alloy nanoparticles (NPs) with tunable magnetization were synthesized by a simple sonofragmentation process, a facile one-step technique to produce NPs directly from bulk powders. The X-ray diffraction (XRD) patterns show the crystalline structure of the alloy samples, and the sizes of the particles are 35 nm from the Scherrer equation. Scanning electron microscopy reveals the aggregation or cluster of spherical NPs with wide size distribution from 20 to 30 nm for all compositions of Ni-Fe nanoalloys. Magnetization versus field curves exhibit superparamagnetic behavior. The saturation magnetization for the $Ni_{0.80}Fe_{0.20}$, $Ni_{0.60}Fe_{0.40}$, and $Ni_{0.20}Fe_{0.80}$ alloy NPs are 57, 66, and 105 emu g^{-1}, respectively, increasing with Fe content. Such tunability has potential technological applications.

Index Terms—Nanomagnetics, Ni–Fe, nanoparticles, nanoalloy, soft magnetic materials, sonofragmentation, saturation magnetization.

I. INTRODUCTION

The development of innovative devices needs novel, small size, low cost, and high characteristic functional materials. Hence, finding new materials of multifunctional properties is always a hot issue to the materials scientist community. In this context, nanoparticles (NPs) have great significance toward practical applications. For this, over the last few decades, the preparation of nanostructures has been attracting considerable interest [Zhou 2015]. Particularly, magnetic NPs are a topic of growing attention because of their versatile applications in magnetic devices, drug delivery, magnetic separation, MRI contrast enhancement, magnetic fluids, hyperthermia, magnetic sensors, catalysis, microwave absorbers, inductor cores, etc. [Schooneveld 2012, Moghimi 2013, Shokuhfar 2014, Kandapallil 2015, Sharma 2015, Zhou 2015, Ishizaki 2016]. In addition, the development of bimetallic NPs (alloy) based on Fe, Co, and Ni has received much recent attention because of their novel catalytic, magnetic, and optical properties, which could be considerably different from those of their constituent single metallic materials [Moghimi 2013, Sharma 2015]. Various properties of alloy can be displayed by changing the composition of the alloy [Basith 2014, Moghimi 2014, Kozhitov 2015]. Moreover, Ni-Fe alloy NPs have attracted significant research interest because of their high magnetic permeability and low hysteresis loss [Ban 2006]. A small variation in the composition of Ni–Fe alloy can cause considerable changes in the magnetic moment and coercivity of the alloy [Wu 2005]. Thus, the controlled composition is a key factor for tuning the magnetic properties of the alloy particles toward desired applications.

Various synthesis methods including hydrothermal, thermal decomposition, microemulsion, solution phase reduction of precursor materials, and wet chemistry have been reported for the synthesis of Ni-Fe NPs [Cushing 2004, Wu 2005, Liao 2006, Wei 2006, Chen 2009]. Although all the above-mentioned methods somehow significantly contribute to synthesize Ni-Fe NPs with various structures, shape, and properties, the use of either complex solution process or involvement of toxic surfactants and high cost still remains a challenge. On the other hand, the sonofragmentation technique is a one-step synthesis technique to produce NPs directly from bulk powder, which is simple, low cost, rapid, and environmental friendly [Basith 2014, Basith 2017]. Hence, sonofragmentation technique could be an alternative cost-effective way to synthesize Ni-Fe nanoalloys.

In this investigation, we have demonstrated a simple cost-effective and nontoxic sonofragmentation technique to synthesize superparamagnetic Ni-Fe alloy NPs. The compositions of the Ni-Fe alloy are varied by changing the precursor concentration to obtain controlled magnetic properties. The morphology, structure, elemental composition, and magnetic properties of the synthesized nanoalloys are investigated by field emission scanning electron microscopy (FE-SEM), X-ray diffraction (XRD), energy-dispersive spectroscopy (EDS), and a vibrating sample magnetometer (VSM), respectively.

II. EXPERIMENTAL DETAILS

A. Materials and Synthesis

The precursor materials of Fe and Ni powder were purchased from Merck KGaA, Germany. 2-isopropanol of analytical grade was also purchased from Merck KGaA, Germany, and used without further purification. Deionized water was used in all the experiments. In a typical synthesis, Fe and Ni powder in stoichiometric proportion were weighed and then mixed together to obtain a homogeneous mixture. After that, the mixture was thoroughly ground by performing manual grinding for approximately 4 h. The obtained mixture powder was further mixed with 2-isopropanol with a ratio of 50 mg powder and

Corresponding authors: Brajalal Sinha and Sri Ramulu Torati (e-mail: brajalal@sh.mist.ac.bd; toratisriramulu@scbt.sastra.edu).
Digital Object Identifier 10.1109/LMAG.2017.2740385

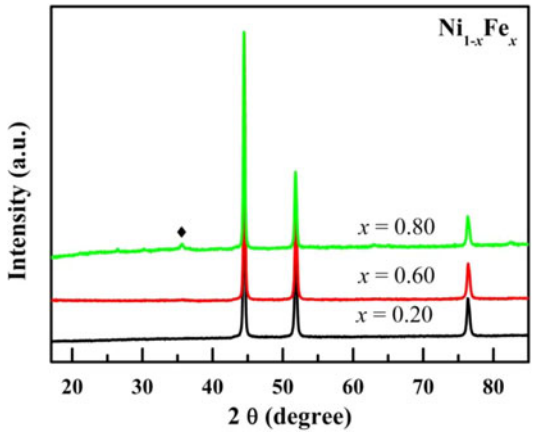

Fig. 1. XRD spectra of $Ni_{1-x}Fe_x$ nanoalloy.

10 ml isopropanol with a mass percentage of ∼0.5%. Then, the mixture of isopropanol and powder was put into ultrasonication bath for 30 min. After 6 h, the precipitant was collected and used for the investigation of structural and magnetic properties.

B. CHARACTERIZATION TECHNIQUES

The crystal structure of the magnetic nanoalloys was characterized using XRD at room temperature (Rigaku Ultimate VII) with CuK_α (1.5418 Å), and the morphological microstructure of the samples was observed by FE-SEM (S-4800, Hitachi) at an operating voltage of 3 kV. The EDS coupled with the FE-SEM was used for the analysis of elemental composition. The operating voltage and probe current for the measurement EDS system was 15 kV and 1.5 nA. The magnetic properties were measured using a VSM at room temperature (VSM, Lakeshore7400series) with a sensitivity of 10^{-6} emu at an applied field range of 10−10 kOe. The VSM measurement of the samples was done after complete drying of the samples.

III. RESULTS AND DISCUSSIONS

The crystallinity of the nanoalloy structures was determined using XRD from 2θ angle values of 20°–80°. Fig. 1 shows the XRD patterns of the three compositions of Ni-Fe nanoalloys. It can be seen from the XRD patterns that the peaks at 44.42°, 51.8°, and 76.2° correspond to the crystal planes of (111), (200), and (220) of face-centered cubic (fcc)$Ni_{1-x}Fe_x$ alloy, respectively, which are in good agreement with already reported literature [Chen 2009, Moghimi 2013, Sharma 2015, Zhou 2015]. However, the XRD spectrum of $Ni_{0.20}Fe_{0.80}$ ($x = 0.80$ in Fig. 1) shows another additional peak at 35.7° (marked with an asterisk) indicating that the obtained alloy cannot be indexed to fcc Ni-Fe alloy. This diffraction peak corresponds to a spinel oxide ($(FeNi)_3O_4$), which indicates that the formation of an oxide phase resulted in a high concentration of Fe precursor [Chen 2009]. Generally, Fe-rich NPs are more easily oxidized, and thus the formation of oxide phase could be obvious [Chen 2009]. No diffraction patterns of pure metallic Fe or Ni are detected, indicating the absence of segregated metal NPs in the alloy samples. The absence of pure Fe or Ni peak in XRD also indicates no phase separation in the bimetallic alloy [Sharma 2015]. Using the Scherrer equation [Patterson 1939, Hall 2000] from the full width at half maximum of the most intense XRD peak (111), the size of the Ni-Fe nanocrystallite was calculated to be 35 nm for all composition. The size of the Ni-Fe nanocrystallite was found to be independent of composition, which indicates uniform fragmentation for a fixed sonication time and power.

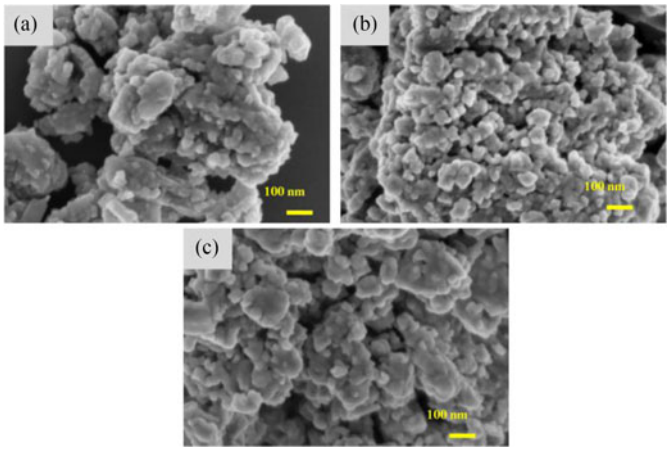

Fig. 2. FE-SEM images of (a) $Ni_{0.80}Fe_{0.20}$, (b) $Ni_{0.60}Fe_{0.40}$, (c) $Ni_{0.20}Fe_{0.80}$.

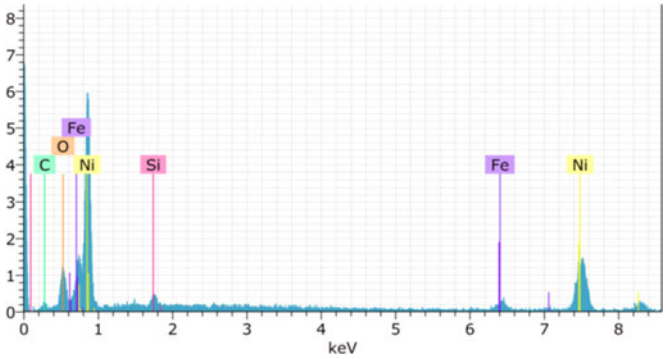

Fig. 3. EDS spectra for $Ni_{0.80}Fe_{0.20}$.

The SEM images of the synthesized Ni-Fe nanoalloy are presented in Fig. 2. From SEM images [see Fig. 2(a)–(c)], it is clear that all Ni-Fe nanoalloy compositions under scrutiny exhibit a wide range of size distribution from 20 to 30 nm with rough surface and spherical shape morphology, and aggregated themselves to a cluster of particles.

The EDS analyses were conducted to obtain corresponding elemental composition of the nanoalloys. Fig. 3 shows a typical EDS spectrum for $Ni_{0.80}Fe_{0.20}$. Both Fe and Ni peaks are apparent in the spectrum. This result also confirmed the formation of Ni-Fe nanoalloy. As shown in Fig. 3, the presence of silicon peak in the EDS spectrum may be due to the SiO_2 substrate used for the sampling of NPs for EDS analysis. The occurrence of the *O* peak may be due to the oxidation of the nanoalloy. However, the XRD data do not show any oxidation peaks for the composition of $Ni_{0.80}Fe_{0.20}$ and $Ni_{0.60}Fe_{0.40}$ alloy, which indicates that there may be very thin or no crystalline oxidation layer on the surface or may be the SiO_2 substrate.

The magnetic properties of Ni-Fe nanoalloy were measured using VSM at room temperature to determine their saturation magnetization (M_s) and coercivity (H_c). Fig. 4 shows the *M–H* curves of $Ni_{1-x}Fe_x$ ($x = 0.2$, 0.6, and 0.8) measured in external magnetic fields ranging from −10 to 10 kOe. From the figure, it can be seen that the Ni-Fe nanoalloys exhibit superparamagnetic behavior. The saturation magnetization increases with the increase of the Fe content in the Ni-Fe

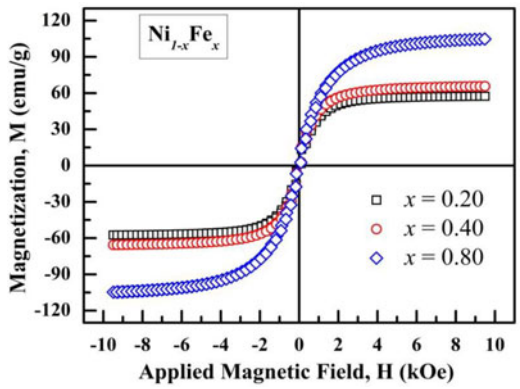

Fig. 4. Magnetization versus magnetic field curves of $Ni_{1-x}Fe_x$ nanoalloy.

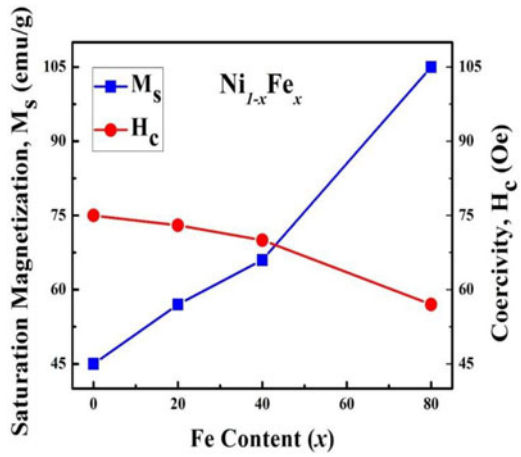

Fig. 5. Variation of saturation magnetization and coercivity with Fe in $Ni_{1-x}Fe_x$ nanoalloy.

alloys (see Fig. 5). However, the coercivity decreases with the increase of the Fe content in the Ni-Fe alloy composition. The increased saturation magnetization is due to the incorporation of higher magnetic moment Fe atoms [Chen 2009]. Moreover, there is a possibility of easy oxidation for more Fe content in the alloy, which was revealed in the XRD patterns. The maximum saturation magnetization and coercivity were estimated to be 105 emu/g and 57 Oe for the composition $Ni_{0.20}Fe_{0.80}$, respectively, as shown in Fig. 3. The decrease of the Fe content in an iron-based binary or ternary alloy decreases the coercivity [Sharma 2015], which is not indicated in Fig 5. Furthermore, in the framework of the Stoner–Wohlfarth model [Stoner 1948], in the ideal case of well-separated fine particles, the M_r/M_s ratio is 0.5. Thus, the fact that the values of the M_r/M_s ratio of synthesized different Ni-Fe nanoalloy composition are found to be lower than 0.5 indicate relatively low interparticle distances between Ni-Fe nanoalloy in all compositions. In addition, it is interesting to note that the presently obtained results show a clear advance with those already reported in the literature, where they used different methods for synthesizing Ni-Fe, as shown in Table 1. Thus, such compositional dependent tunable magnetic properties of the Ni-Fe alloy can be used for various applications. The potential applications of the presently prepared nanoalloy are currently under investigation in various relative fields of nanomaterials and nanotechnology.

TABLE 1. Comparative study of reported magnetic properties of Ni-Fe nanoalloys prepared by using different synthesis methods.

Composition	M_s (emug)	H_c (Oe)	Synthesis Method	Refs.
Ni-Fe	97	250	Template based self-assembly	Zhou 2015
	69–90	150–100	Non-aqueous organometallic route	Chen 2009
	85, 40	100, 188	Coelectrodiposition	Moghimi 2014
	110	100	Hydrazine reduction	Lu 2007
	57–105	73–57	Sonofragmentation	Present work

IV. CONCLUSION

In summary, a facile and cost-effective sonofragmentated approach for the synthesis of Ni-Fe nanoalloys with various compositions of Fe and Ni is demonstrated successfully. We used only the ultrasonic energy for the fragmentation of bigger particles, and no additional reducing or reacting agents are used for the synthesis of alloy NPs. SEM results showed that the nanoalloy particles are aggregated in nature with wide size distribution. Although, further work is required to control particle size and shape, it is an initiation of the use of sonofragmentation technique for the synthesis of nanoalloy which is cost effective, toxic surfactant free, and environmental friendly. Significant modifications in the magnetic properties are obtained by changing the composition of the Ni-Fe nanoalloy. In particular, the saturation magnetization increases with the increased Fe content in the Ni–Fe alloy. Furthermore, a half-time reduced coercivity of the reported value is found for $Fe_{80}Ni_{20}$ composition than other composition of the Ni-Fe alloy. The synthesized high magnetization Ni-Fe nanoalloy can be used for various potential applications, and also this simple technique can be extended to synthesize other nanoalloys.

ACKNOWLEDGMENT

This work was supported by the World Academy of Sciences, Italy under Grant 14-024 RG/PHY/AS_I-UNESCO FR: 324028590.

REFERENCES

Ban I, Drofenik M, Markovec D (2006), "The synthesis of iron-nickel alloy nanoparticles using a reverse micelle technique," *J. Magn. Magn. Mater.*, vol. 307, pp. 250–256, doi: 10.1016/j.jmmm.2006.04.010.

Basith M A, Islam M A, Ahmmad B, Hossain Md S, Mølhave K (2017), "Preparation of high crystalline nanoparticles of rare-earth based complex perovskites and comparison of their structural and magnetic properties with bulk counterparts," *Mater. Res. Express*, vol. 4, 075012, doi: 10.1088/2053-1591/aa769e.

Basith M A, Ngo D-T, Quader A, Rahman M A, Sinha B L, Ahmad B, Hirose F, Molhave K (2014), "Simple top-down preparation of magnetic $Bi_{0.9}Gd_{0.1}Fe_{1-x}Ti_xO_3$ nanoparticles by ultrasonication of multiferroic bulk material," *Nanoscale*, vol. 6, pp. 14336–14342, doi: 10.1039/c4nr03150d.

Chen Y, Luo X, Yue G H, X Luo, Peng D L (2009), "Synthesis of iron–nickel nanoparticles via a nonaqueous organometallic route," *Mater. Chem. Phys.*, vol. 113, pp. 412–416, doi: 10.1016/j.matchemphys.2008.07.118.

Cushing B L, Golub V, O'Connor C J (2004), "Synthesis and magnetic properties of Au-coated amorphous $Fe_{20}Ni_{80}$ nanoparticles," *J. Phys. Chem. Solids* vol. 65, pp. 825–829, doi: 10.1016/j.jpcs.2003.11.027

Hall B D, Zachet D, Ugarte D (2000), "Estimating nanoparticle size from diffraction measurements," *J. Appl. Crystallography*, vol. 33, pp. 1335–1311, doi: 10.1107/S0021889800010888.

Ishizaki T, Yatsugi K, Akedo K (2016), "Effect of particle size on the magnetic properties of Ni nanoparticles synthesized with trioctylphosphine as the capping agent," *Nanomaterials*, vol. 6, 172. doi: 10.3390/nano6090172.

Kandapallil B, Colborn R E, Bonitatibus P J, Johnson F (2015), "Synthesis of high magnetization Fe and FeCo nanoparticles by high temperature chemical reduction," *J. Magn. Magn. Mater.*, vol. 378, pp. 535–538, doi: 10.1016/j.jmmm.2014.11.074.

Kozhitov L V, Bulatov M F, Korovushkin V V, Kostisshin V G, Muratov D G, Shipko M N, Emelyanov S G, Yakushko E V (2015), "The formation and study of the FeCo nanoparticles alloy in structure of metal-carbon nanocomposites FeCo/C," *J. Nano Electron. Phys.*, vol. 7, 04103. [Online]. Available: http://jnep.sumdu.edu.ua:8080/component/search/index.php?option=com_content&task=full_article&id=1715

Liao Q, Tannenbaum R, Wang Z L (2006), "Synthesis of $FeNi_3$ alloyed nanoparticles by hydrothermal reduction," *J. Phys. Chem. B*, vol. 110, pp. 14262–14265, doi: 10.1021/jp0625154.

Lu X, Liang G, Zhang Y (2007), "Synthesis and characterization of magnetic $FeNi_3$ particles obtained by hydrazine reduction in aqueous solution" *Mater. Sci. Eng. B*, vol. 139, pp. 124–127. doi: 10.1016/j.mseb.2007.01.055.

Moghimi N, Bazargan S, Pradhan D, Leung K T (2013), "Phase-induced shape evolution of FeNi nanoalloys and their air stability by in-situ surface passivation," *J. Phys. Chem. C*, vol. 117, pp. 4852–4858, doi: 10.1021/jp312391h.

Moghimi N, Rahsepar F R, Srivastava S, Heinig N, Leung K T (2014), "Shape-dependent magnetism of bimetallic FeNi nanosystems," *J. Mater. Chem. C*, vol. 2, pp. 6370–6375, doi: 10.1039/c4tc00443d.

Patterson A L (1939), "The Scherrer formula for X-ray particle size determination," *Phys. Rev.*, vol. 56, pp. 978–982, doi: 10.1103/PhysRev.56.978.

Schooneveld M M V, Campos-Cuerva C, Pet J, Meeldijk J D, Rijssel J V, Meijerink A, Erne B H, Groot F M F D (2012), "Composition tunable cobalt-nickel and cobalt-iron alloy nanoparticles below 10 nm synthesized using acetonated cobalt carbonyl," *J. Nanoparticle Res.*, vol. 14, 991. doi: 10.1007/s11051-012-0991-5.

Sharma H, Jain S, Raj P M, Murali K P Tummala R (2015), "Magnetic and dielectric property studies in Fe- and NiFe- based polymer nanocomposites," *J. Electron. Mater.*, vol. 44, , pp. 3819–3826, doi: 10.1007/s11664-015-3801-x.

Shokuhfar A, Afghahi S S S (2014), "Size controlled synthesis of FeCo nanoparticles and study of the particle size and distribution effects on magnetic properties," *Adv. Mater. Sci. Eng.*, 2014, 295390, doi: 10.1155/2014/295390.

Stoner E C, Wohlfarth E P (1948), "A mechanism of magnetic hysteresis in heterogeneous alloys," *Phil. Trans. Roy. Soc. London Ser. A*, vol. 240, pp. 599–642, doi: 10.1098/rsta.1948.0007.

Wei X W, Zhu G X, Zhou J H, Sun H Q (2006), "Solution phase reduction to Fe–Ni alloy nanostructures with tunable shape and size," *Mater. Chem. Phys.*, vol. 100, pp. 481–485, doi: 10.1016/j.matchemphys.2006.01.030.

Wu H Q, Cao Y J, Yuan P S, Xu H Y, Wei X W (2005), "Controlled synthesis, structure and magnetic properties of $Fe_{1-x}Ni_x$ alloy nanoparticles attached on carbon nanotubes," *Chem. Phys. Lett.*, vol. 406, pp. 148–153, doi: 10.1016/j.cplett.2005.02.117.

Zhou J, Jiao T, Guo W, Wang B, Guo H, Cui L, Zhang Q, Chen Y Peng Q (2015), "Preparation of iron-nickel alloy nanostructures via two cationic pyridinium derivatives as soft templates," *Nanomater. Nanotechnol.*, vol. 5, 25, doi: 10.5772/61296.